Chapter 4

PLL-less Control Strategy of a Grid-Tied PV System Under Distorted Grid Voltage Conditions

4.1 Introduction

An advanced proportional multi-resonant (APMR) current controller integrated with a compensator for grid voltage sag (CGVS) has been discussed in the previous chapter. The combination of APMR and CGVS has been operated in a coordinated manner to suppress grid current harmonics and power ripples simultaneously under distorted grid voltage conditions. However, due to the presence of a synchronization unit, phase-locked loop (PLL), the implementation complexity and computational burden on the digital controller increases. In view of the aforementioned points, the requirement of a PLL-less control strategy is realized. This chapter presents a PLL-less control strategy for a three-phase grid-tied PV system that mitigates grid current harmonics and power ripples simultaneously. The proposed PLL-less control strategy consists of APMR current controller in integration with a phase compensated reference current generator (PCRCG), which suppresses the harmonics currents and eliminates the power oscillations under distorted grid voltage conditions. The synchronization task is included in the proposed PCRCG, which makes the overall system PLL-less. Thus, the associated computational burden and implementation complexities on the digital controller is reduced. Further, the frequency adaptability of the grid-tied PV system is enhanced as compared to the PLL-based control strategy in the presence of grid frequency variations using the proposed control strategy. The effectiveness of the proposed control strategy is compared with the conventional PLL-based control strategy using OPAL-RT real-time digital simulator.

4.2 System Architecture of PLL-less Grid-Tied PV System

The system architecture of the single-stage grid-tied PV system with the proposed PLL-less control strategy is shown in Fig. 4.1. It consists of a PV array connected to the grid at the point of interconnection with a VSI and LCL filter. In the LCL filter; L_{if} and L_{of} represents the inductors of the inverter and grid side; R_{if} and R_{of} are the resistors of the inverter and grid sides and C_{f} and R_{c} denotes the shunt branch capacitor and resistor of the LCL filter. The equivalent inductor and resistor of the grid are indicated as L_{g} and R_{g} respectively. The structure of the grid-tied PV PLL-less control scheme is divided into four parts, which are: i) adaptive step size INC (ASINC) MPPT controller, ii) DC-link voltage controller, iii) advanced proportional multi-resonant (APMR) current controller and (iv) phase compensated reference current generator (PCRCG). The PV array voltage of the system is decided by the reference DC-link voltage, which is determined by the ASINC MPPT controller. The PCRCG has two important features, which are: i) it removes the PLL block and provides the reference value of grid current in $\alpha\beta$ reference frame without grid phase angle information ii) it mitigates the active and reactive power ripples under unbalanced grid voltage (voltage sag and swell) conditions. The APMR current controller uses the reference grid currents generated by the PCRCG and use them to mitigates grid current harmonics under the distorted grid voltage conditions. The VSI is automatically synchronized to the grid without a dedicated synchronization unit such as PLL. A detailed discussion of the proposed PLL-less scheme of APMR current controller with PCRCG is presented in section 4.3. The other associated primary controllers, i.e., MPPT and DC-link voltage controller are discussed in the following subsections.

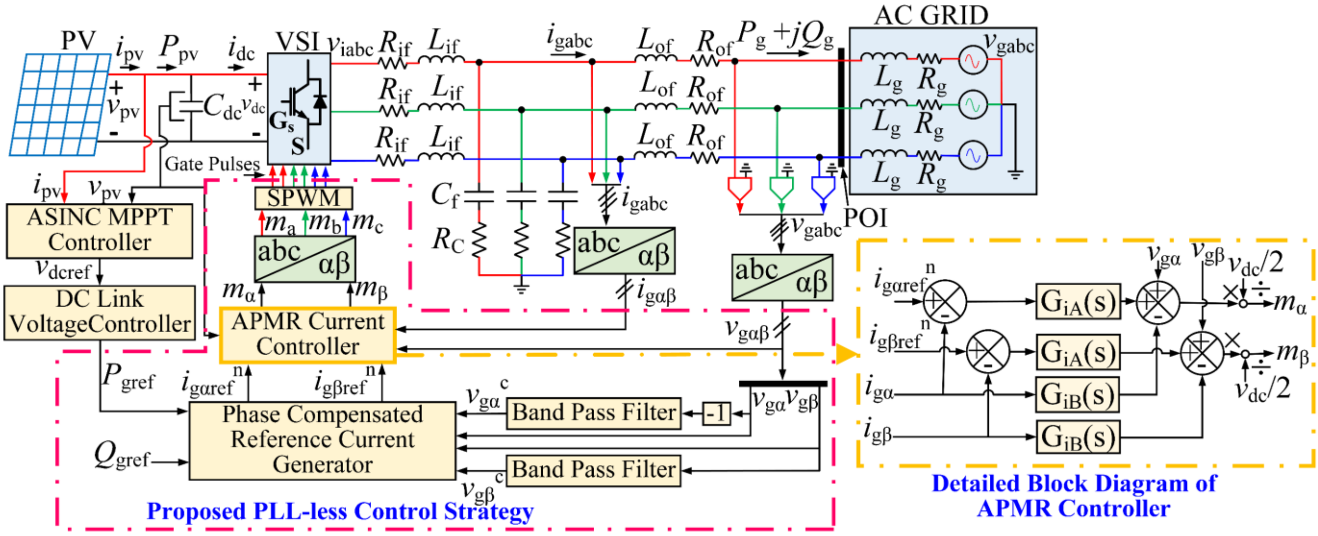

Fig. 4.1. The proposed PLL-less control strategy architecture for grid-tied PV system.

4.2.1 Adaptive Step Size INC MPPT Controller Design

In the case of the fixed step size incremental conductance (FSINC) MPPT method, there is a trade-off between steady-state oscillations and power losses around MPP due to larger step size and larger MPP tracking speed due to smaller step size. Many researchers have tried to solve this problem through some modifications in the FSINC MPPT methods. However, the combination of proportional resonant (PR) controller with MPPT for simultaneous mitigation of the grid current harmonics and extraction of maximum power from the PV array has not been attempted till date. For harmonic minimization, the PR-based controller's implementation has a payoff in terms of transients introduced, which increases the settling time. Therefore, the tracking is not proper in case of the FSINC method with a small MPPT sampling time (0.02 s). For proper MPPT with FSINC, the required sampling time increases (0.06 s) and thus the total tracking time increases. Therefore, to take care of such design issues, an adaptive step size incremental conductance (ASINC) MPPT method is presented in [106] with variable voltage step size and MPPT sampling time (0.06 s). The ASINC MPPT is used with the proposed control strategy to achieve faster-tracking speed and better MPP tracking accuracy under variable environmental conditions. The voltage step size of the ASINC MPPT method is adaptively varied, based on the rate of change of power with voltage dp_{PV}/dv_{PV} in voltage versus power characteristics of the PV array. When the PV system’s operating point is far from the MPP, the ASINC MPPT is adapted for fast and smooth MPP tracking with a larger step size. If the operating point is near the MPP, the minimum step size prevents negligible oscillations at MPP. The pictorial representation of the ASINC MPPT algorithm is illustrated in Fig. 4.2. The variable step size V_{st} is calculated according to the PV power and voltage variations as follows:

$$V_{st} = k\left|\frac{v_{PV}(t)i_{PV}(t) - v_{PV}(t-1)i_{PV}(t-1)}{v_{PV}(t) - v_{PV}(t-1)}\right| \tag{4.1}$$

where $v_{pv}(t)$, $i_{pv}(t)$, $v_{pv}(t-1)$ and $i_{pv}(t-1)$ are PV voltages and currents at t th and (t-1) th iterations. The scaling coefficient of the ASINC method to adjust the step size is represented as k.

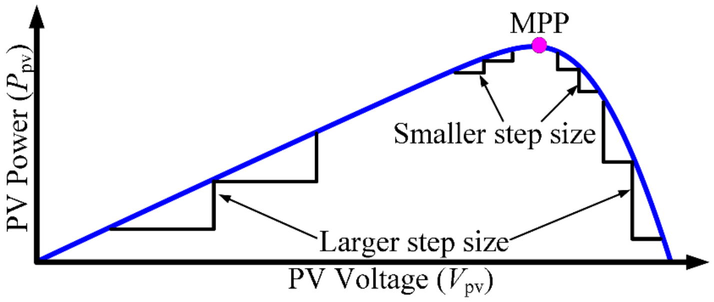

Fig. 4.2. Pictorial representation of MPP tracking with ASINC MPPT controller.

4.2.2 DC link Voltage Controller Modelling

The DC link voltage controller’s primary goal is to control the DC-link voltage by stabilizing the DC power from the PV array. The block diagram of the DC-link voltage controller is shown in Fig. 4.3. The voltage dynamics of the DC-link capacitor is expressed as

$$\frac{d}{dt}(0.5C_{\mathrm{dc}}{v_{\mathrm{dc}}}^2) = P_{\mathrm{PV}} - P_{\mathrm{g}} \tag{4.2}$$

where C_{dc} is the DC-link capacitor and v_{dc} is voltage across it. P_{PV} is the PV array DC power and P_{g} is the active power injected into the grid. The P_{PV} can be expressed as

$$P_{\mathrm{PV}} = v_{\mathrm{dc}} i_{\mathrm{dc}} = v_{\mathrm{PV}} i_{\mathrm{PV}} \tag{4.3}$$

where v_{PV}, i_{PV} and i_{dc} are the PV array voltage, PV array current and the current flowing in the DC side of the VSI.

Substituting (4.3) in (4.2),

$$C_{\mathrm{dc}}\frac{dv_{\mathrm{dc}}}{dt} = i_{\mathrm{PV}} - \frac{P_{\mathrm{g}}}{v_{\mathrm{dc}}} \tag{4.4}$$

According to the FBL technique, (4.4) can be expressed as

$$C_{\mathrm{dc}}\frac{dv_{\mathrm{dc}}}{dt} = u_{\mathrm{dc}} \tag{4.5}$$

where u_{dc} is the new control input. A controller $G_{\mathrm{c}}^{\mathrm{vdc}}$ based on a conventional PI controller is applied to maintain the DC-link voltage v_{dc} according to its reference value v_{dcref}. The output of the voltage controller is used as power reference P_{gref} for the PCRCG.

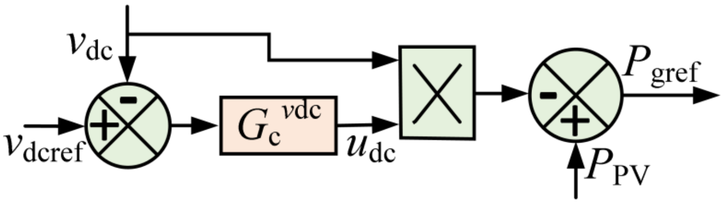

Fig. 4.3. Block diagram of the DC link voltage control.

4.3 PLL-Based Control Strategy

The PLL-based conventional proportional multi resonant (CPMR) control strategy uses the basic concept of the resonant controller for regulating the grid current harmonics. The control structure block diagram of the PLL-based CPMR control strategy is shown in Fig. 4.4. The current reference i_{gdref} and i_{gqref} of the CPMR controller are obtained from the output of the DC-link voltage controller and reactive power loop block, respectively. The PLL-based CPMR control strategy requires accurate phase information of the fundamental component of grid voltage. This information is obtained from the PLL with grid voltages as input and then generates the phase information (in the form of phase angle) as output. The phase angle of the grid θ_{PLL} obtained from SRF-PLL (discussed in chapter 3) is used for the coordinate transformation from *dq* frame to *αβ* frame. The grid current $i_{\mathrm{g\propto ref}}$ and

$i_{g\beta ref}$ are obtained from *dq* to *αβ* transformation block. The error between the reference grid currents ($i_{g\propto ref}$ and $i_{g\beta ref}$) and the measured grid currents ($i_{g\propto}$ and $i_{g\beta}$) are processed by the proportional resonant compensator (PRC) G_{iAc}(s) and resonant harmonic compensator (RHC) G_{iBc}(s) connected in parallel. The PRC ensures the accurate tracking of the fundamental component of grid current reference and the RHC compensates the selected grid current harmonics. The transfer function of G_{iAc}(s) and G_{iBc}(s) are expressed as

$$\left.\begin{aligned} G_{iAc}(s) &= K_p + \frac{K_{rA}s}{s^2+\omega_g{}^2} \\ G_{iBc}(s) &= \sum_{n=5}^{h} \frac{K_{rB}s}{s^2+(n\omega_g)^2} \end{aligned}\right\} \tag{4.6}$$

where k_p is the proportional coefficient; k_{rA} and k_{rB} are the resonant coefficients of the CPMR controller; ω_g and *n* are the resonant frequency and harmonic order of the CPMR controller. The output of the CPMR controller gives the modulation signals m_α and m_β. Again these signals are transformed to m_{abc} and used in SPWM to generate the gating signals for switching of VSI.

4.4 Proposed PLL-Less Control Strategy

This section introduces a PLL-less control strategy for a three-phase grid-tied PV system. The APMR controller along with PCRCG are operated in a coordinated way to suppress the grid current harmonics under harmonically distorted grid voltage conditions and eliminate the active and reactive power ripples under unbalanced grid voltage sags and swells. The description of the APMR controller and its frequency response analysis are given in section 4.4.1. The mathematical description of active and reactive power oscillations under unbalanced grid voltages are discussed in section 4.4.2. The PCRCG for suppressing the active and reactive power oscillations is described in detail through mathematical formulation in section 4.4.3.

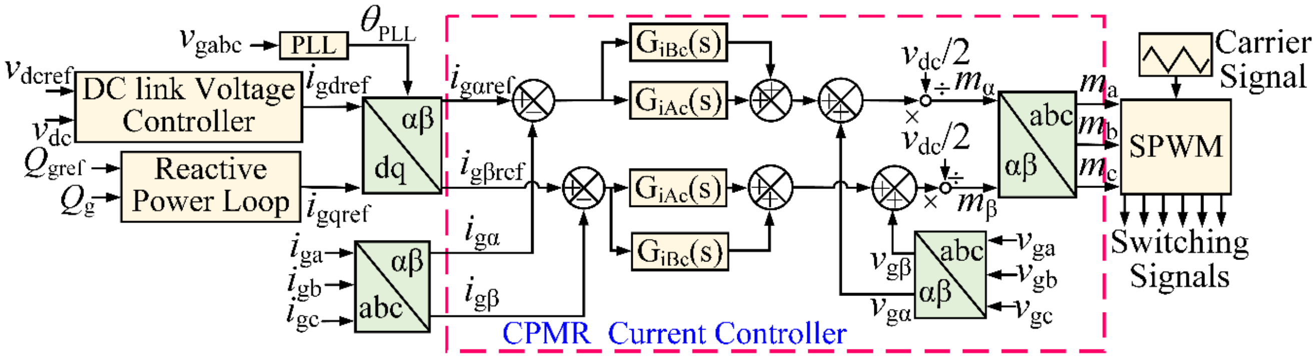

Fig. 4.4. Block diagram of PLL-based CPMR control strategy.

4.4.1 Proposed PLL-less APMR Controller

The proposed PLL-less APMR controller regulates the fundamental grid injected current and mitigates the harmonics under distorted grid voltage conditions for a grid-tied PV system. Moreover, the APMR controller supports robust and faster dynamic response under grid frequency variations and minimizes the steady-state error at the fundamental frequency. The block diagram of the APMR current controller is illustrated in Fig. 4.5. Its input current reference in *αβ* domain is obtained from PCRCG. The proposed APMR controller consists of two parallel branches which are: *i*) proportional resonant controller (PRC) and *ii*) multi resonant harmonic controller (MRHC). The PRC with transfer function $G_{\mathrm{iA}}(s)$ exhibits excellent performance while tracking and controlling the grid-tied PV system's fundamental current. The MRHC with transfer function $G_{\mathrm{iB}}(s)$ is used to suppress the selected harmonics injected into the grid. The transfer function of G_{iA} (s) and G_{iB} (s) are expressed as

$$\left.\begin{aligned} G_{\mathrm{iA}}(s) &= \frac{2K_{\mathrm{rA}}\omega_{\mathrm{b}}s}{s^2+2\omega_{\mathrm{b}}s+\omega_{\mathrm{g}}{}^2} \\ G_{\mathrm{iB}}(s) &= K_{\mathrm{p}}+\sum_{\mathrm{n=5}}^{\mathrm{h}}\frac{2K_{\mathrm{rB}}(n\omega_{\mathrm{b}})s}{s^2+2(n\omega_b)s+(n\omega_{\mathrm{g}})^2} \end{aligned}\right\} \tag{4.7}$$

where K_{p} is the proportional coefficient; K_{rA} and K_{rB} are the resonant coefficients of the APMR controller; ω_{b} and ω_{g} are the bandwidth and resonant frequency of the APMR controller ($\omega_{\mathrm{b}} = \xi\omega_{\mathrm{g}}$); ξ and *n* are the damping coefficient and harmonic order.

The APMR controller is used to regulate the grid current reference value by processing the grid current error $i_{\mathrm{g\alpha\beta ref}}$ -$i_{\mathrm{g\alpha\beta}}$ applied to the input of $G_{\mathrm{iA}}(s)$. The injected grid current $i_{\mathrm{g\alpha\beta}}$ is applied to the input of $G_{\mathrm{iB}}(s)$ as shown in Fig. 4.5. The output of the APMR controller is multiplied by $2/v_{\mathrm{dc}}$ to generate the modulating signals for the VSI. The flow chart of the proposed PLL-less APMR control strategy for the grid tied PV system is shown in Fig. 4.6.

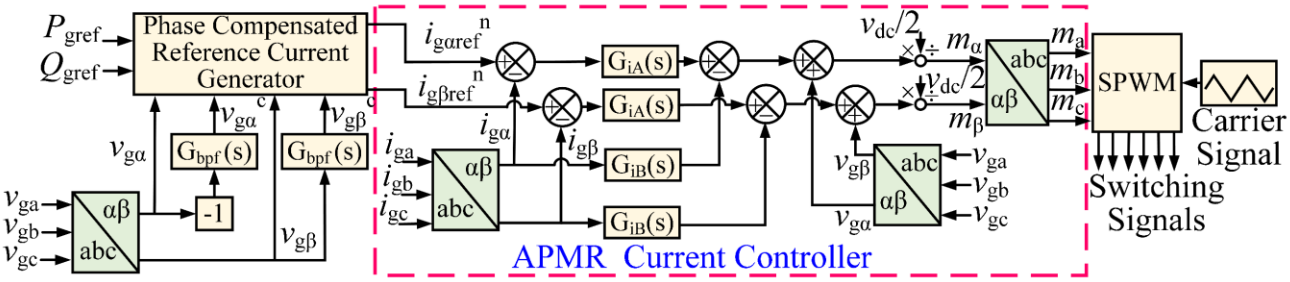

Fig. 4.5. Block diagram of the proposed PLL-less APMR control strategy.

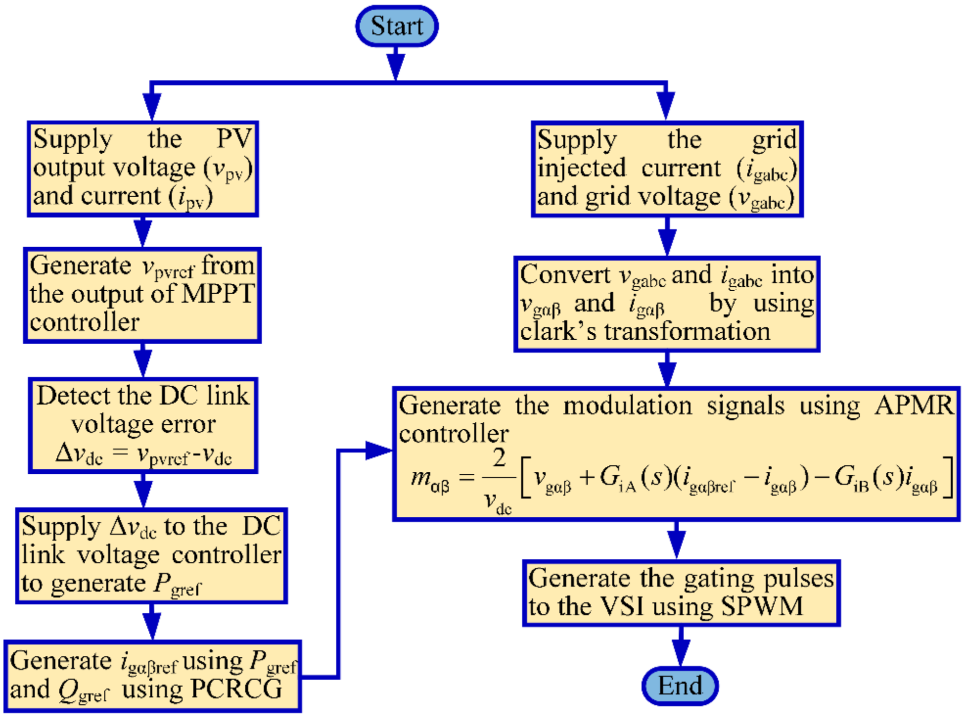

Fig. 4.6. Flowchart of the proposed PLL-less APMR control strategy.

4.4.1.1 Frequency Response Analysis of the Proposed APMR Controller

To investigate the proposed APMR controller's capability in compensating the grid current harmonics, the frequency response of the closed-loop control system is analyzed in this section, which is discussed in a similar way in chapter 3. A three-phase grid-connected VSI can be modeled as an equivalent circuit as shown in Fig. 4.7. The $\alpha\beta$ component of the inverter output voltage is expressed as

$$v_{i\alpha\beta} = \frac{v_{dc}}{2} m_{\alpha\beta} \tag{4.8}$$

where $v_{i\alpha\beta}$ is the $\alpha\beta$ component of inverter output voltage, v_{dc} is DC-link voltage and $m_{\propto\beta}$ is the modulation signals of the VSI obtained from the output of the APMR controller. Z_{if}, and Z_{cf} denote the series impedance of filter at the inverter side and shunt impedance of the filter; Z_{of} and Z_g are series impedance of filter at the grid side and the equivalent grid impedance. The impedances are expressed as $Z_{if} = R_{if} + sL_{if}$, $Z_{of} = R_{of} + sL_{of}$, $Z_{cf} = R_c + 1/sC$ and $Z_g = R_g + sL_g$

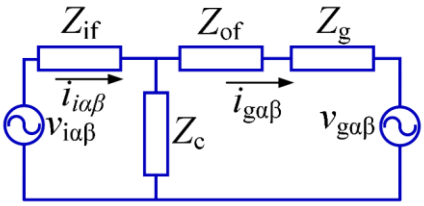

Fig. 4.7. Equivalent circuit of the VSI integrated to the grid in the *αβ* reference frame.

From Fig. 4.5, the modulation signals of the VSI in the *αβ* reference frame can be written as

$$m_{\mathrm{\alpha\beta}} = \frac{2}{v_{\mathrm{dc}}}\left[v_{\mathrm{g\alpha\beta}} + G_{\mathrm{iA}}(s)(i_{\mathrm{g\alpha\beta ref}} - i_{\mathrm{g\alpha\beta}}) - G_{\mathrm{iB}}(s)i_{\mathrm{g\alpha\beta}}\right] \tag{4.9}$$

From the expression given in s (4.8), (4.9) and Fig. 4.7, the inverter voltage $v_{\mathrm{i\alpha\beta}}$, grid voltage $v_{\mathrm{g\alpha\beta}}$ and the inverter current $i_{\mathrm{i\alpha\beta}}$ can be expressed as

$$v_{\mathrm{i\alpha\beta}} = \frac{2}{m_{\mathrm{\alpha\beta}}}\left(Z_{\mathrm{if}}(s)i_{\mathrm{i\alpha\beta}} + Z_{\mathrm{c}}(s)(i_{\mathrm{i\alpha\beta}} - i_{\mathrm{g\alpha\beta}})\right) \tag{4.10}$$

$$v_{\mathrm{g\alpha\beta}} = \frac{v_{\mathrm{i\alpha\beta}}}{2} - Z_{\mathrm{if}}(s)i_{\mathrm{i\alpha\beta}} - \left\{Z_{\mathrm{g}}(s) + Z_{of}(s)\right\}i_{\mathrm{g\alpha\beta}} \tag{4.11}$$

$$i_{\mathrm{i\alpha\beta}} = \left(\frac{\left\{Z_{\mathrm{of}}(s) + Z_{\mathrm{g}}(s)\right\}i_{\mathrm{g\alpha\beta}} + v_{\mathrm{g\alpha\beta}}}{Z_{\mathrm{c}}(s)}\right) + i_{\mathrm{g\alpha\beta}} \tag{4.12}$$

By substituting (4.10) - (4.12) in (4.9), the closed-loop transfer function $G_{\mathrm{i\text{-}cl}}$(s) of the reference grid current $i_{\mathrm{g\alpha\beta ref}}$ with respect to the actual grid current $i_{\mathrm{g\alpha\beta}}$ is expressed as

$$G_{\mathrm{i\text{-}cl}}(s) = \frac{i_{\mathrm{g\alpha\beta ref}}}{i_{\mathrm{g\alpha\beta}}} = \frac{Z_{\mathrm{c}}(s)G_{\mathrm{iA}}(s)G_{\mathrm{f}}(s)}{1 + T(s)} \tag{4.13}$$

where *T*(s) is the open-loop gain of the APMR current controller. The transfer function $G_{\mathrm{i\text{-}cl}}$ (s) is used to analyze the grid current harmonic rejection capability. The open-loop gain *T*(s) and the transfer function G_{f} (s) are given by

$$T(s) = \left\{Z_{\mathrm{cf}}(s) + Z_{\mathrm{of}}(s) + Z_{\mathrm{g}}(s)\right\}\left\{G_{\mathrm{iA}}(s) + G_{\mathrm{iB}}(s)\right\}G_{\mathrm{del}}(s)G_{\mathrm{f}}(s) \tag{4.14}$$

$$G_{\mathrm{f}}(s) = \frac{1}{Z_{\mathrm{if}}(s)\left\{Z_{\mathrm{cf}}(s) + Z_{\mathrm{of}}(s) + Z_{\mathrm{g}}(s)\right\} + Z_{\mathrm{cf}}(s)\left\{Z_{\mathrm{of}}(s) + Z_{\mathrm{g}}(s)\right\}} \tag{4.15}$$

4.4.1.2 Selection and Influence of Control Parameters of the Proposed APMR Controller

This section discusses the selection and influence of control parameters to achieve a satisfactory reduction in grid current harmonics. It can be noticed from (4.7) that the APMR controller has four adjustable control parameters K_p, K_{rA}, K_{rB} and ω_b (= ξ ω_g). The bode diagrams of $G_{i\text{-}cl}(s)$ obtained using different K_p, K_{rA}, K_{rB} and ξ are illustrated in Fig.4.8. Fig. 4.8(a) shows the bode diagrams of $G_{i\text{-}cl}(s)$, when $K_p = 60$, $K_{rA} = K_{rB} = 360$ and ξ varies. It is noticed from Fig. 4.8(a) that with the increase in ξ, the peak disappears from the Bode diagram's of $G_{i\text{-}cl}(s)$. Thus, the attenuation of lower order harmonics reduces. Therefore, the smaller value of ξ is used for effective harmonic compensation. The Bode diagram of the closed-loop transfer function $G_{i\text{-}cl}(s)$ for the APMR controller with different K_r and fixed K_p and ξ is illustrated in Fig. 4.8(b). It is seen from Fig. 4.8(b) that as the value of K_{rA} and K_{rB} increase, the peak magnitude at the resonant frequency (50 Hz) increases. The larger values of K_{rA} and K_{rB} are used to provide better steady-state performance for harmonic current compensation. It is noticed from Fig. 4.8(c) that by keeping K_{rA}, K_{rB} and ξ fixed, the variation of K_P directly influences the magnitude and phase response of $G_{i\text{-}cl}(s)$. It is observed that with the increase in the value of $K_{p,}$ the peak value decreases in the magnitude plot.

The selection of control parameters K_p, K_{rA}, K_{rB} and $\omega_b = \xi\ \omega_g$ is vital during the design and implementation of the APMR controller. For the optimal control coefficients of APMR controller the design steps are as follows:

Step1(selection of ω_b*)*: To achieve armonic compensation, an approximate value of ξ is selected to find ω_b. According to the power quality standards [121], the value of ω_b is expressed as

$$\omega_b = 2 * \pi * f_g * \xi \tag{4.16}$$

where f_g and ξ are the grid frequency and the damping coefficient, respectively.

Step2 (selection of K_p*)*: With the possible values of switching frequency (f_s), inverter side inductance (L_{if}) and the grid side inductance (L_{of}), the value of K_p is calculated as follows

$$K_p = \frac{f_s(L_{if} + L_{of})}{3} \tag{4.17}$$

Step3 (selection of K_{rA} *and* K_{rB}*)*: With the obtained K_p, the values of K_{rA} and K_{rB} can be calculated as follows [122]

$$K_{rA} = K_{rB} = \frac{K_p(R_{if} + R_{of})}{L_{if} + L_{of}} \tag{4.18}$$

where R_{if} and R_{of} are the inverter side and grid side resistances, respectively.

By selecting the values of $f_s = 20$ kHz, $L_{if} = 6.2$ mH, $L_{of} = 1.6$ mH, $R_{if} = 0.037\ \Omega$ and $R_{of} = 0.016\ \Omega$ and using (4.17) and (4.18), K_p=52, K_{rA}=354 and K_{rB}=354. In the experimental study, $K_p = 60$, $K_{rA} = 360$ and $K_{rB} = 360$ to avoid the transient oscillations. The values of $\xi = 0.02$.

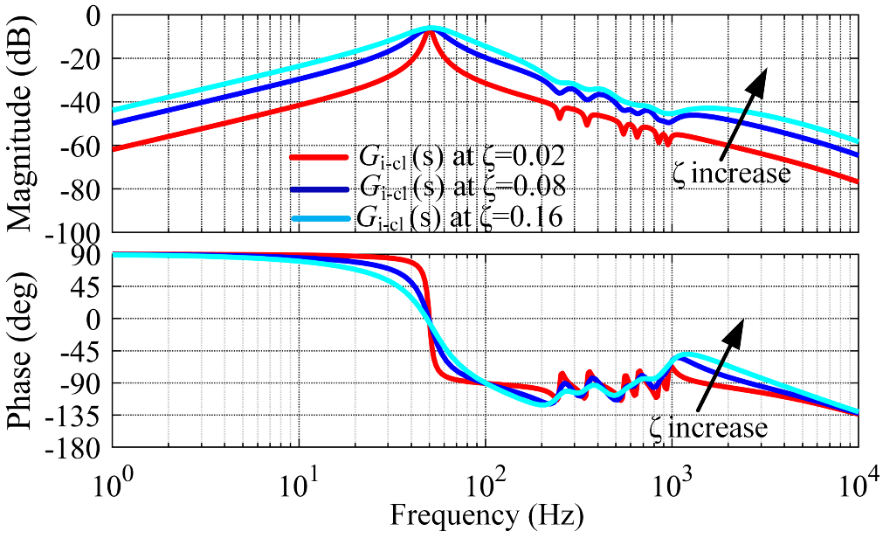

(a)

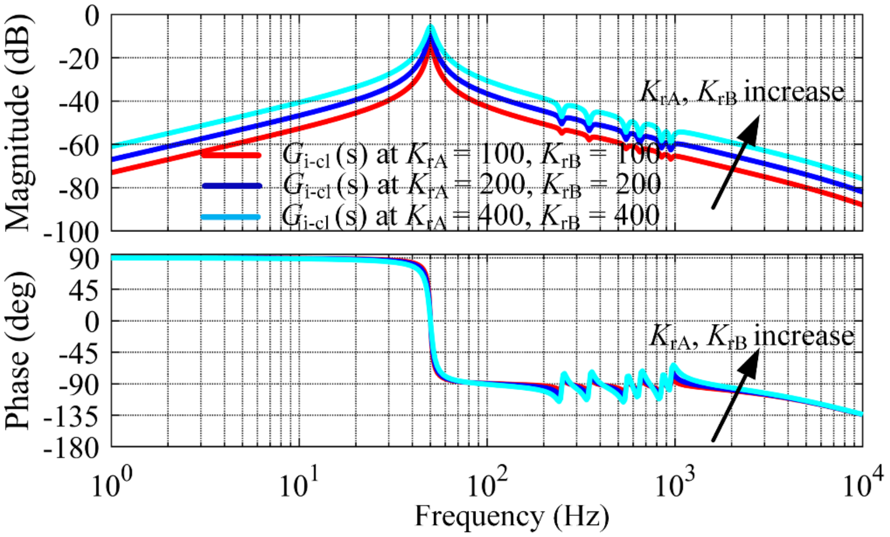

(b)

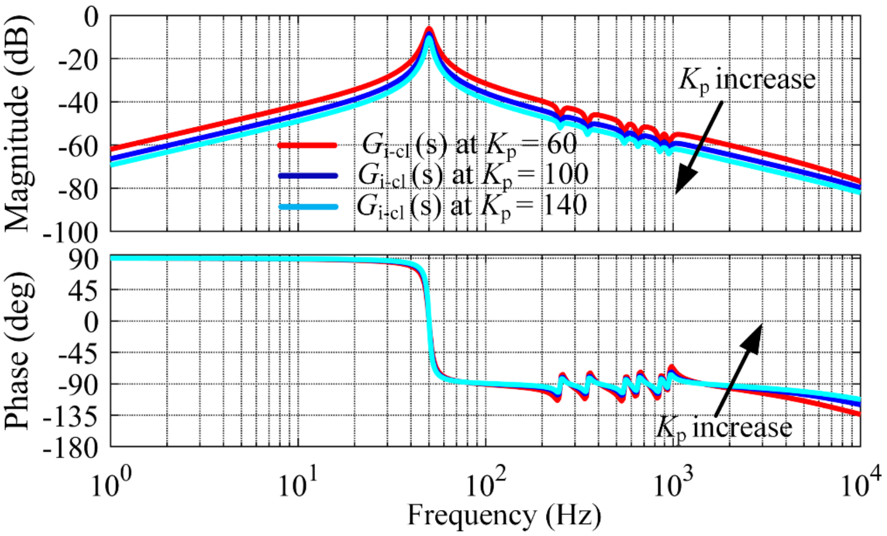

(c)

Fig. 4.8. The Bode diagram of the closed loop transfer function $G_{i\text{-}cl}(s)$ with different K_p ,K_{rA}, K_{rB} and ξ . (a) K_p= 60, K_{rA}= 360, K_{rB}=360 and ξ = 0.02,0.08 and 0.16. (b) K_p= 60, K_{rA}= 100,200, 400 K_{rB}=100,200 and 400, and ξ = 0.02. (c) K_p= 60,100 and 140, K_{rA}= 360, K_{rB}= 360, and ξ = 0.02.

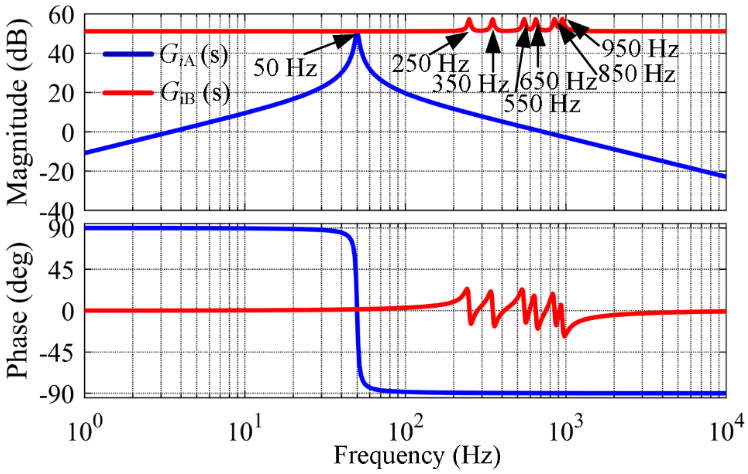

Fig. 4.9. The Bode diagram of $G_{iA}(s)$ and $G_{iB}(s)$ of the APMR controller with K_p= 60, K_{rA}= 360, K_{rB} = 360, and ζ =0.02.

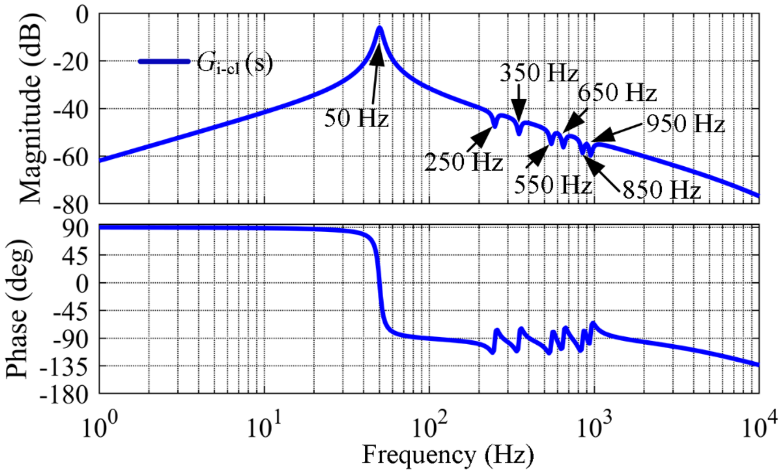

Fig. 4.10. The Bode diagram of the closed-loop transfer function $G_{i\text{-}cl}(s)$ with K_p= 60, K_{rA}= 360, K_{rB}= 360, and ζ =0.02.

The Bode diagram of $G_{iA}(s)$ and $G_{iB}(s)$ of the APMR controller are illustrated in Fig. 4.9. It is observed that the magnitude of $G_{iA}(s)$ at the resonant frequency is more than 40 dB and the peaks appear in G_{iB} (s) at the selected harmonic frequencies 250 Hz, 350 Hz, 550 Hz,650 Hz, 850 Hz and 950 Hz for the selected harmonics 5th,7th,11th,13th,17th and 19th. Since the output of the transfer function $G_{iB}(s)$ is subtracted from the output of transfer function $G_{iA}(s)$ as shown in Fig. 4.5, the APMR removes the selected harmonics from the output of $G_{iA}(s)$. Consequently, the reference modulating signal m_{abc} obtained at the output of the proposed APMR controller contains reduced magnitudes of lower order harmonics. The Bode diagram of the closed-loop transfer function $G_{i\text{-cl}}$ (s) of the reference grid current $i_{g\alpha\beta ref}$ with respect to the actual grid current $i_{g\alpha\beta}$ of the APMR controller is shown in Fig. 4.10. It is observed that the magnitude and phase of $G_{i\text{-cl}}(s)$ at the fundamental grid frequency that the gain is unity and the phase shift is zero, indicating a satisfactory steady-state reference tracking. Moreover, at the selective harmonic frequencies 250 Hz, 350 Hz, 550 Hz,650 Hz, 850 Hz and 950 Hz the magnitude response of $G_{i\text{-cl}}(s)$ is significantly attenuated. Therefore, the proposed APMR controller mitigates the lower order harmonics.

4.4.2 Active and Reactive Power Oscillations Under Unbalanced Grid Voltages

Under the unbalanced grid voltage conditions (unbalanced grid voltage sag and swell), both the positive and negative sequence components appear in the grid voltage. Due to the negative sequence component in the voltage, the generated reference current also consists of negative sequence component causing a negative sequence current. This negative sequence current is injected into the grid. The interaction between these sequence components of grid voltages and currents generates active and reactive power oscillations. These active and reactive power oscillations deteriorate the power quality of the grid-tied PV system. Such power oscillations lead to current and voltage ripples on the DC-link and this may create instability in the grid-tied PV system. To mitigate these power ripples, PCRCG is presented and discussed in detail in section 4.4.3. The three-phase unbalanced grid voltage can be expressed as

$$\begin{bmatrix} v_{ga} \\ v_{gb} \\ v_{gc} \end{bmatrix} = \begin{bmatrix} v_{ga}^{+} \\ v_{gb}^{+} \\ v_{gc}^{+} \end{bmatrix} + \begin{bmatrix} v_{ga}^{-} \\ v_{gb}^{-} \\ v_{gc}^{-} \end{bmatrix} = \begin{bmatrix} V_{p}\sin(\omega t+\theta_{p})+V_{n}\sin(\omega t+\theta_{n}) \\ V_{p}\sin(\omega t+\theta_{p}-120)+V_{n}\sin(\omega t+\theta_{n}-120) \\ V_{p}\sin(\omega t+\theta_{p}+120)+V_{n}\sin(\omega t+\theta_{n}+120) \end{bmatrix} \tag{4.19}$$

where V_p and V_n represent the positive and negative sequences voltage magnitudes; θ_p and θ_n represent the positive and negative sequences phase angles and ω represents the angular frequency. Using Clark's transformation in (4.19), the grid voltage v_{gabc} can be transferred to $v_{\mathrm{g}\alpha}$ and $v_{\mathrm{g}\beta}$ as follows [123]

$$\left.\begin{aligned}
&\begin{bmatrix} v_{\mathrm{g}\alpha} \\ v_{\mathrm{g}\beta} \end{bmatrix} = \frac{2}{3}\begin{bmatrix} 1 & -\frac{1}{2} & -\frac{1}{2} \\ 0 & \frac{\sqrt{3}}{2} & -\frac{\sqrt{3}}{2} \end{bmatrix}\begin{bmatrix} v_{\mathrm{ga}} \\ v_{\mathrm{gb}} \\ v_{\mathrm{gc}} \end{bmatrix} = \begin{bmatrix} v_{\mathrm{g}\alpha}{}^{+} \\ v_{\mathrm{g}\beta}{}^{+} \end{bmatrix} + \begin{bmatrix} v_{\mathrm{g}\alpha}{}^{-} \\ v_{\mathrm{g}\beta}{}^{-} \end{bmatrix} \\
&\begin{bmatrix} v_{\mathrm{g}\alpha}{}^{+} \\ v_{\mathrm{g}\beta}{}^{+} \end{bmatrix} = \begin{bmatrix} V_{\mathrm{p}}\sin(\omega t+\theta_{p}) \\ -V_{\mathrm{p}}\cos(\omega t+\theta_{p}) \end{bmatrix} \\
&\begin{bmatrix} v_{\mathrm{g}\alpha}{}^{-} \\ v_{\mathrm{g}\beta}{}^{-} \end{bmatrix} = \begin{bmatrix} V_{\mathrm{n}}\sin(\omega t+\theta_{n}) \\ V_{\mathrm{n}}\cos(\omega t+\theta_{n}) \end{bmatrix}
\end{aligned}\right\} \tag{4.20}$$

where $v_{\mathrm{g}\alpha}{}^{+}$, $v_{\mathrm{g}\alpha}{}^{-}$, $v_{\mathrm{g}\beta}{}^{+}$ and $v_{\mathrm{g}\beta}{}^{-}$ are the positive and negative sequence components of $v_{\mathrm{g}\alpha}$ and $v_{\mathrm{g}\beta}$ in $\alpha\beta$ reference frame.

The instantaneous active power P_{g} and reactive power Q_{g} injected to the grid can be expressed as

$$\begin{bmatrix} P_{\mathrm{g}} \\ Q_{\mathrm{g}} \end{bmatrix} = \frac{3}{2}\begin{bmatrix} v_{\mathrm{g}\alpha} & v_{\mathrm{g}\beta} \\ v_{\mathrm{g}\beta} & -v_{\mathrm{g}\alpha} \end{bmatrix}\begin{bmatrix} i_{\mathrm{g}\alpha} \\ i_{\mathrm{g}\beta} \end{bmatrix} \tag{4.21}$$

The reference current value $\mathrm{i}_{\mathrm{g}\alpha\mathrm{ref}}$ and $i_{\mathrm{g}\beta\mathrm{ref}}$ based on the P_{gref}, Q_{gref}, $v_{\mathrm{g}\alpha}$ and $v_{\mathrm{g}\beta}$ can be derived from (4.21). The active and reactive power current components can be decomposed as

$$\left.\begin{aligned}
&\begin{bmatrix} i_{\mathrm{g}\alpha\mathrm{ref}} \\ i_{\mathrm{g}\beta\mathrm{ref}} \end{bmatrix} = \frac{2}{3}\begin{bmatrix} v_{\mathrm{g}\alpha} & v_{\mathrm{g}\beta} \\ v_{\mathrm{g}\beta} & -v_{\mathrm{g}\alpha} \end{bmatrix}^{-1}\begin{bmatrix} P_{\mathrm{gref}} \\ Q_{\mathrm{gref}} \end{bmatrix} \\
&\begin{bmatrix} i_{\mathrm{g}\alpha\mathrm{ref}} \\ i_{\mathrm{g}\beta\mathrm{ref}} \end{bmatrix} = \begin{bmatrix} i_{\mathrm{g}\alpha\mathrm{ref\,(p)}} \\ i_{\mathrm{g}\beta\mathrm{ref\,(p)}} \end{bmatrix} + \begin{bmatrix} i_{\mathrm{g}\alpha\mathrm{ref\,(q)}} \\ i_{\mathrm{g}\beta\mathrm{ref\,(q)}} \end{bmatrix} \\
&\qquad = \frac{2}{3}\frac{P_{\mathrm{gref}}}{\mathrm{v}_{\mathrm{g}\alpha}{}^{2}+\mathrm{v}_{\mathrm{g}\beta}{}^{2}}\begin{bmatrix} v_{\mathrm{g}\alpha} \\ v_{\mathrm{g}\beta} \end{bmatrix} + \frac{2}{3}\frac{Q_{\mathrm{gref}}}{v_{\mathrm{g}\alpha}{}^{2}+v_{\mathrm{g}\beta}{}^{2}}\begin{bmatrix} v_{\mathrm{g}\beta} \\ -v_{\mathrm{g}\alpha} \end{bmatrix}
\end{aligned}\right\} \tag{4.22}$$

where P_{gref} and Q_{gref} are the active and the reactive power references injected into the grid, and $i_{\mathrm{g}\alpha\mathrm{ref(p)}}$, $i_{\mathrm{g}\beta\mathrm{ref(p)}}$, $i_{\mathrm{g}\alpha\mathrm{ref(q)}}$ and $i_{\mathrm{g}\beta\mathrm{ref(q)}}$ represent the reference active and reactive power current component in $\alpha\beta$ reference frame. By substituting (4.20) in (4.22), $i_{\mathrm{g}\alpha\mathrm{ref(p)}}$, $i_{\mathrm{g}\beta\mathrm{ref(p)}}$, $i_{\mathrm{g}\alpha\mathrm{ref(q)}}$ and $i_{\mathrm{g}\beta\mathrm{ref(q)}}$ can be obtained as follows

$$\left.\begin{aligned}
&\begin{bmatrix} i_{\mathrm{g}\alpha\mathrm{ref\,(p)}} \\ i_{\mathrm{g}\beta\mathrm{ref\,(p)}} \end{bmatrix} = \frac{2}{3}\frac{P_{\mathrm{gref}}}{(v_{\mathrm{g}\alpha}{}^{+}+v_{\mathrm{g}\alpha}{}^{-})^{2}+(v_{\mathrm{g}\beta}{}^{+}+v_{\mathrm{g}\beta}{}^{-})^{2}}\begin{bmatrix} v_{\mathrm{g}\alpha}{}^{+}+v_{\mathrm{g}\alpha}{}^{-} \\ v_{\mathrm{g}\beta}{}^{+}+v_{\mathrm{g}\beta}{}^{-} \end{bmatrix} \\
&\begin{bmatrix} i_{\mathrm{g}\alpha\mathrm{ref\,(q)}} \\ i_{\mathrm{g}\beta\mathrm{ref\,(q)}} \end{bmatrix} = \frac{2}{3}\frac{Q_{\mathrm{gref}}}{(v_{\mathrm{g}\alpha}{}^{+}+v_{\mathrm{g}\alpha}{}^{-})^{2}+(v_{\mathrm{g}\beta}{}^{+}+v_{\mathrm{g}\beta}{}^{-})^{2}}\begin{bmatrix} v_{\mathrm{g}\alpha}{}^{+}+v_{\mathrm{g}\alpha}{}^{-} \\ v_{\mathrm{g}\beta}{}^{+}+v_{\mathrm{g}\beta}{}^{-} \end{bmatrix}
\end{aligned}\right\} \tag{4.23}$$

By further simplifying (4.23),

$$\left.\begin{aligned}
i_{\mathrm{g\alpha ref\,(p)}} &= \frac{2}{3}\,\frac{P_{\mathrm{gref}}\,v_{\mathrm{g\alpha}}}{(V_{\mathrm{p}})^2+(V_{\mathrm{n}})^2-2V_{\mathrm{p}}V_{\mathrm{n}}\cos(2\omega t+\theta_p+\theta_n)}\\
i_{\mathrm{g\alpha ref\,(q)}} &= \frac{2}{3}\,\frac{Q_{\mathrm{gref}}\,v_{\mathrm{g\beta}}}{(V_{\mathrm{p}})^2+(V_{\mathrm{n}})^2-2V_{\mathrm{p}}V_{\mathrm{n}}\cos(2\omega t+\theta_p+\theta_n)}\\
i_{\mathrm{g\beta ref\,(p)}} &= \frac{2}{3}\,\frac{P_{\mathrm{gref}}\,v_{\mathrm{g\beta}}}{(V_{\mathrm{p}})^2+(V_{\mathrm{n}})^2-2V_{\mathrm{p}}V_{\mathrm{n}}\cos(2\omega t+\theta_p+\theta_n)}\\
i_{\mathrm{g\beta ref\,(q)}} &= -\frac{2}{3}\,\frac{Q_{\mathrm{gref}}\,v_{\mathrm{g\alpha}}}{(V_{\mathrm{p}})^2+(V_{\mathrm{n}})^2-2V_{\mathrm{p}}V_{\mathrm{n}}\cos(2\omega t+\theta_p+\theta_n)}
\end{aligned}\right\}\tag{4.24}$$

It is observed that $i_{\mathrm{g\propto ref(p)}}$, $i_{\mathrm{g\beta ref(p)}}$, $i_{\mathrm{g\propto ref(q)}}$ and $i_{\mathrm{g\beta ref(q)}}$ in (4.24) contain lower-order harmonics due to the presence of double grid frequency oscillation $2V_{\mathrm{p}}V_{\mathrm{n}}\cos(2\omega \mathrm{t}+\theta_{\mathrm{p}}+\theta_{\mathrm{n}})$. Therefore, a notch filter is used to suppress the lower order harmonics by canceling the terms $2V_{\mathrm{p}}V_{\mathrm{n}}\cos(2\omega \mathrm{t}+\theta_{\mathrm{p}}+\theta_{\mathrm{n}})$ in (4.24). The transfer function of the notch filter $G_{\mathrm{nf}}(\mathrm{s})$ is expressed as

$$\mathrm{G_{nf}(s)}=\frac{\mathrm{s}^2+\omega_{\mathrm{n}}{}^2}{\mathrm{s}^2+2\delta\omega_{\mathrm{n}}\mathrm{s}+\omega_{\mathrm{n}}{}^2}\tag{4.25}$$

where ω_{n} and $\delta\omega_n$ are the notch and cut-off frequencies of the notch filter. The active and reactive power current references of (4.24) can be rewritten as

$$\left.\begin{aligned}
i_{\mathrm{g\alpha ref\,(p)}} &= \frac{2}{3}\,\frac{P_{\mathrm{gref}}\,v_{\mathrm{g\alpha}}}{\left[(v_{\mathrm{g\alpha}})^2+(v_{\mathrm{g\beta}})^2\right]G_{\mathrm{nf}}(\mathrm{s})}=\frac{2}{3}\,\frac{P_{\mathrm{gref}}\,v_{\mathrm{g\alpha}}}{(V_{\mathrm{p}})^2+(V_{\mathrm{n}})^2}\\
i_{\mathrm{g\alpha ref\,(q)}} &= \frac{2}{3}\,\frac{Q_{\mathrm{gref}}\,v_{\mathrm{g\beta}}}{\left[(v_{\mathrm{g\alpha}})^2+(v_{\mathrm{g\beta}})^2\right]G_{\mathrm{nf}}(\mathrm{s})}=\frac{2}{3}\,\frac{Q_{\mathrm{gref}}\,v_{\mathrm{g\beta}}}{(V_{\mathrm{p}})^2+(V_{\mathrm{n}})^2}\\
i_{\mathrm{g\beta ref\,(p)}} &= \frac{2}{3}\,\frac{P_{\mathrm{gref}}\,v_{\mathrm{g\beta}}}{\left[(v_{\mathrm{g\alpha}})^2+(v_{\mathrm{g\beta}})^2\right]G_{\mathrm{nf}}(\mathrm{s})}=\frac{2}{3}\,\frac{P_{\mathrm{gref}}\,v_{\mathrm{g\beta}}}{(V_{\mathrm{p}})^2+(V_{\mathrm{n}})^2}\\
i_{\mathrm{g\beta ref\,(q)}} &= -\frac{2}{3}\,\frac{Q_{\mathrm{gref}}\,v_{\mathrm{g\alpha}}}{\left[(v_{\mathrm{g\alpha}})^2+(v_{\mathrm{g\beta}})^2\right]G_{\mathrm{nf}}(\mathrm{s})}=-\frac{2}{3}\,\frac{Q_{\mathrm{gref}}\,v_{\mathrm{g\alpha}}}{(V_{\mathrm{p}})^2+(V_{\mathrm{n}})^2}
\end{aligned}\right\}\tag{4.15}$$

It is noted that the notch filter eliminates the term $2V_{\mathrm{p}}V_{\mathrm{n}}\cos(2\omega \mathrm{t}+\theta_{\mathrm{p}}+\theta_{\mathrm{n}})$ from (4.15). By substituting (4.15) in (4.10) and (4.11), the active power injected into the grid is calculated by considering $\mathrm{i}_{\mathrm{g\propto ref(p)}}$ and $i_{\mathrm{g\beta ref(p)}}$. Similarly, the reactive power injected into the grid is calculated by considering $i_{\mathrm{g\propto ref(q)}}$ and $i_{\mathrm{g\beta ref(q)}}$. The active power P_{gosc} and reactive power Q_{gosc} can be expressed as

$$\left.\begin{aligned}P_{\text{gosc}} &= \frac{P_{\text{gref}}}{(V_{\text{p}})^2+(V_{\text{n}})^2}\left[(v_{\text{g}\alpha})^2+(v_{\text{g}\beta})^2\right]\\ &= P_{\text{gref}} - \frac{2P_{\text{gref}}V_{\text{p}}V_{\text{n}}}{(V_{\text{p}})^2+(V_{\text{n}})^2}\cos(2\omega t+\theta_p+\theta_n)\\ &= P_{\text{gref}}+P_{\text{g}2\omega}\\ Q_{\text{gosc}} &= \frac{Q_{\text{gref}}}{(V_{\text{p}})^2+(V_{\text{n}})^2}\left[(v_{\text{g}\alpha})^2+(v_{\text{g}\beta})^2\right]\\ &= Q_{\text{gref}} - \frac{2Q_{\text{gref}}V_{\text{p}}V_{\text{n}}}{(V_{\text{p}})^2+(V_{\text{n}})^2}\cos(2\omega t+\theta_p+\theta_n)\\ &= Q_{\text{gref}}+Q_{\text{g}2\omega}\end{aligned}\right\} \tag{4.16}$$

It is noticed from (4.16) that there are oscillations components of $\cos(2\omega t+\theta_{\text{p}}+\theta_{\text{n}})$ in P_{gosc} and Q_{gosc} with twice the grid frequency components. A balanced and sinusoidal grid current is obtained at the expense of active and reactive power oscillations. Therefore, there is a trade-off between the lower-order current harmonics and power oscillations. Due to the oscillations in P_{gosc}, the DC-link voltage at the input side of VSI also oscillates at twice the grid frequency. These undesirable oscillations in DC-link voltage may cause overvoltage and instability in the DC-link voltage (PV voltage). Further, these oscillations degrade the system performance of the grid-tied PV system by reducing the power efficiency of the PV array, deteriorate the output power quality, increase the power losses of the grid-tied PV system, shorten the life span of PV panels and DC-link capacitor. Moreover, due to the reactive power oscillations, there is a rise in the grid current and thus the power losses in the grid-tied PV system increase [124]. The DC-link voltage ripple is expressed as

$$\text{v}_{\text{dc}2\omega} = \frac{\text{P}_{\text{g}2\omega}}{\omega \text{C}_{\text{dc}}\text{V}_{\text{dc}}} \tag{4.17}$$

where $v_{\text{dc}2\omega}$ and $P_{\text{g}2\omega}$ are the magnitudes of the second-order oscillating DC-link voltage and second-order oscillating active power, V_{dc} is the rated DC-link voltage across the DC-link capacitor C_{dc}. The DC-link capacitor voltage oscillations are reduced by mitigating of active power oscillations, which can be achieved by cancelling the term $\cos(2\omega t+\theta_{\text{p}}+\theta_{\text{n}})$ from (4.16).

4.4.3 Phase Compensated Reference Current Generator

In order to take care of the issues mentioned in section 4.4.2, a PCRCG is presented in this section. The PCRCG is an essential block of a PLL-less grid-tied PV system for generating the reference currents $i_{\text{g}\alpha\text{ref}}$ and $i_{\text{g}\beta\text{ref}}$ for the current controller with input references as grid injected active power P_g, reactive power Q_g and grid voltages $v_{g\alpha}$ and $v_{g\beta}$. The PCRCG reduces the grid-injected current imbalance and eliminates the active and reactive power ripples under unbalanced grid voltage conditions. The block diagram of PCRCG is shown in Fig. 4.11. The PCRCG is a modified form of RCG [123], which consists of a bandpass filter (BPF) and the grid voltages $v_{g\alpha}$ and $v_{g\beta}$ in $\alpha\beta$ reference frame. The PCRCG is used to generate the $\alpha\beta$ components of the reference grid current, which are used in the APMR controller (discussed in section 4.4.1). Further, PCRCG reduces the lower order harmonics in the reference grid currents $i_{g\alpha ref}$ and $i_{g\beta ref}$ and, consequently eliminates the power ripples from the grid. The reference grid currents are generated by using the reference active power P_{gref}, reactive power Q_{gref} and the grid voltages $v_{g\alpha}$, $v_{g\beta}$ in α and β reference frames without using any synchronization tools such as PLLs. The PCRCG and APMR are implemented in the $\alpha\beta$ reference frame, and thus eliminate the need of PLL. The PCRCG and APMR are integrated into a compact structure and operated in a coordinated manner to control the grid-tied PV system. Thus, the synchronization task is included within the PCRCG, which makes the grid-tied PV system PLL-less.

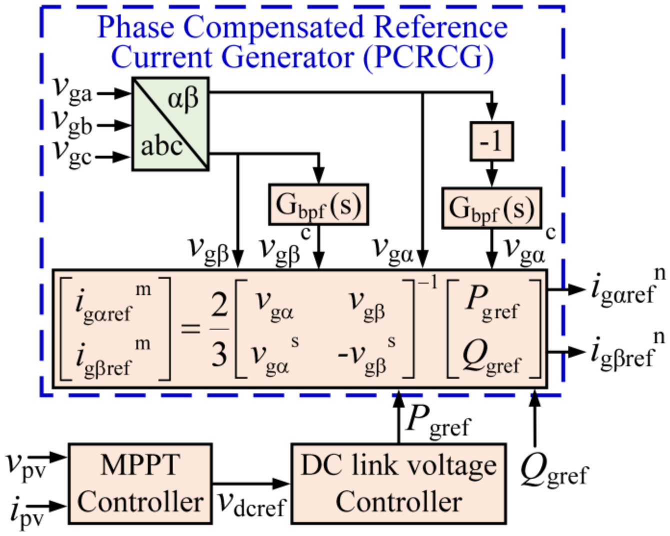

Fig. 4.11. Block diagram of PCRCG.

The reference active power P_{gref} and reactive power Q_{gref} can be expressed as

$$\begin{bmatrix} P_{gref} \\ Q_{gref} \end{bmatrix} = \frac{3}{2}\begin{bmatrix} v_{g\alpha} & v_{g\beta} \\ -v_{g\alpha}G_{bpf}(s) & v_{g\beta}G_{bpf}(s) \end{bmatrix}\begin{bmatrix} i_{g\alpha ref}^n \\ i_{g\beta ref}^n \end{bmatrix} = \frac{3}{2}\begin{bmatrix} v_{g\alpha} & v_{g\beta} \\ v_{g\alpha}^c & -v_{g\beta}^c \end{bmatrix}\begin{bmatrix} i_{g\alpha ref}^n \\ i_{g\beta ref}^n \end{bmatrix} \tag{4.18}$$

where $v_{g\alpha}^c$ and $v_{g\beta}^c$ are the α and β grid voltage components compensated by 135° and 45° phase angle shift in $v_{g\alpha}$ and $v_{g\beta}$. $i_{g\alpha ref}^n$ and $i_{g\beta ref}^n$ denote the α and β compensated grid current references. $G_{bpf}(s)$ is the TF of BPF and is used for the phase compensation in $v_{g\alpha}$ and $v_{g\beta}$. The transfer function of BPF $G_{bpf}(s)$ is expressed as

$$G_{\text{bpf}}(\text{s}) = \frac{2\omega_{\text{c}}\text{s}}{\text{s}^2 + 2\omega_{\text{c}}\text{s} + \omega_{\text{o}}^2} \tag{4.19}$$

where ω_{c} and ω_{o} represent the resonance bandwidth and the resonance frequency of the BPF ($\omega_{\text{c}}=\delta\omega_o$). The value of ω_{o} is set as the grid frequency (50 Hz). For the better dynamic performance of the system, δ is set at 1.

The $v_{\text{g}\propto}$ and $\text{v}_{\text{g}\beta}$ are passed through the BPF for achieving a phase compensation of 135° in $\text{v}_{\text{g}\propto}$ using $-G_{\text{bpf}}(\text{s})$ and 45° in $\text{v}_{\text{g}\beta}$ using $G_{\text{bpf}}(\text{s})$. By doing so, the lower order harmonics that are present in the unbalanced grid voltages of $i_{\text{g}\propto\text{ref}}^{\text{n}}$ and $i_{\text{g}\beta\text{ref}}^{\text{n}}$ are eliminated. Consequently, the active and reactive power oscillations are eliminated. The compensated grid voltage $v_{\text{g}\propto}^{\text{c}}$ and $\text{v}_{\text{g}\beta}^{\text{c}}$ are expressed as

$$\begin{bmatrix} v_{\text{g}\alpha}^{\text{c}} \\ v_{\text{g}\beta}^{\text{c}} \end{bmatrix} = \begin{bmatrix} V_{\text{p}}\sin(\omega t+\theta_p-135) \\ -V_{\text{p}}\cos(\omega t+\theta_p+45) \end{bmatrix} + \begin{bmatrix} V_{\text{n}}\sin(\omega t+\theta_n-135) \\ V_{\text{n}}\cos(\omega t+\theta_n+45) \end{bmatrix} \tag{4.20}$$

The compensated injected current references $i_{\text{g}\propto\text{ref}}^{\text{n}}$ and $i_{\text{g}\beta\text{ref}}^{\text{n}}$ are obtained from (4.18) as

$$\left.\begin{aligned}
&\begin{bmatrix} i_{\text{g}\alpha\text{ref}}^{\text{n}} \\ i_{\text{g}\beta\text{ref}}^{\text{n}} \end{bmatrix} = \frac{2}{3}\begin{bmatrix} v_{\text{g}\alpha} & v_{\text{g}\beta} \\ v_{\text{g}\alpha}^{\text{c}} & -v_{\text{g}\beta}^{\text{c}} \end{bmatrix}^{-1}\begin{bmatrix} P_{\text{gref}} \\ Q_{\text{gref}} \end{bmatrix} = \begin{bmatrix} i_{\text{g}\alpha\text{ref (p)}}^{\text{n}} + i_{\text{g}\alpha\text{ref (q)}}^{\text{n}} \\ i_{\text{g}\beta\text{ref (p)}}^{\text{n}} + i_{\text{g}\beta\text{ref (q)}}^{\text{n}} \end{bmatrix} \\
&i_{\text{g}\alpha\text{ref (p)}}^{\text{n}} = \frac{2}{3}\frac{P_{\text{gref}}v_{\text{g}\beta}^{\text{c}}}{v_{\text{g}\alpha}v_{\text{g}\beta}^{\text{c}} + v_{\text{g}\alpha}^{\text{c}}v_{\text{g}\beta}} = \frac{2}{3}\frac{P_{\text{gref}}v_{\text{g}\beta}^{\text{c}}}{(V_{\text{p}})^2-(V_{\text{n}})^2} \\
&i_{\text{g}\alpha\text{ref (q)}}^{\text{n}} = \frac{2}{3}\frac{Q_{\text{gref}}v_{\text{g}\beta}}{v_{\text{g}\alpha}v_{\text{g}\beta}^{\text{c}} + v_{\text{g}\alpha}^{\text{c}}v_{\text{g}\beta}} = \frac{2}{3}\frac{Q_{\text{gref}}v_{\text{g}\beta}}{(V_{\text{p}})^2-(V_{\text{n}})^2} \\
&i_{\text{g}\beta\text{ref (p)}}^{\text{n}} = \frac{2}{3}\frac{P_{\text{gref}}v_{\text{g}\alpha}^{\text{c}}}{v_{\text{g}\alpha}v_{\text{g}\beta}^{\text{c}} + v_{\text{g}\alpha}^{\text{c}}v_{\text{g}\beta}} = \frac{2}{3}\frac{P_{\text{gref}}v_{\text{g}\alpha}^{\text{c}}}{(V_{\text{p}})^2-(V_{\text{n}})^2} \\
&i_{\text{g}\beta\text{ref (q)}}^{\text{n}} = -\frac{2}{3}\frac{Q_{\text{gref}}v_{\text{g}\alpha}}{v_{\text{g}\alpha}v_{\text{g}\beta}^{\text{c}} + v_{\text{g}\alpha}^{\text{c}}v_{\text{g}\beta}} = \frac{2}{3}\frac{Q_{\text{gref}}v_{\text{g}\alpha}}{(V_{\text{p}})^2-(V_{\text{n}})^2}
\end{aligned}\right\} \tag{4.21}$$

It can be noticed that the denominator in (4.21) has a constant term $(V_{\text{p}})^2-(V_{\text{n}})^2$. Therefore, the second-order components $\cos(2\omega t+\theta_{\text{p}}+\theta_{\text{n}})$ are eliminated. The instantaneous modified active and reactive powers can be obtained as

$$\begin{bmatrix} P_{\text{g mod}} \\ Q_{\text{g mod}} \end{bmatrix} = \frac{3}{2}\begin{bmatrix} v_{\text{g}\alpha} & v_{\text{g}\beta} \\ v_{\text{g}\alpha}^{\text{c}} & -v_{\text{g}\beta}^{\text{c}} \end{bmatrix}\begin{bmatrix} i_{\text{g}\alpha\text{ref}}^{\text{n}} \\ i_{\text{g}\beta\text{ref}}^{\text{n}} \end{bmatrix} \tag{4.22}$$

By substituting (4.21) in (4.22), the modified active and reactive powers can be expressed as

$$\left.\begin{aligned} P_{\mathrm{g\,mod}} &= P_{\mathrm{gref}}\left[\frac{v_{\mathrm{g\alpha}} v_{\mathrm{g\beta}}{}^{\mathrm{c}} + v_{\mathrm{g\alpha}}{}^{\mathrm{c}} v_{\mathrm{g\beta}}}{(V_{\mathrm{p}})^2 - (V_{\mathrm{n}})^2}\right] = P_{\mathrm{gref}}\,\frac{(V_{\mathrm{p}})^2 - (V_{\mathrm{n}})^2}{(V_{\mathrm{p}})^2 - (V_{\mathrm{n}})^2} \\ Q_{\mathrm{g\,mod}} &= Q_{\mathrm{gref}}\left[\frac{v_{\mathrm{g\alpha}}{}^{\mathrm{c}} v_{\mathrm{g\beta}} - v_{\mathrm{g\alpha}} v_{\mathrm{g\beta}}{}^{\mathrm{c}}}{(V_{\mathrm{p}})^2 - (V_{\mathrm{n}})^2}\right] = Q_{\mathrm{gref}}\,\frac{(V_{\mathrm{p}})^2 - (V_{\mathrm{n}})^2}{(V_{\mathrm{p}})^2 - (V_{\mathrm{n}})^2} \end{aligned}\right\} \tag{4.23}$$

It is noticed from (4.23) that there is no oscillations term $\cos(2\omega t+\theta_{\mathrm{p}}+\theta_{\mathrm{n}})$ in P_{gmod} and Q_{gmod}. Therefore, it is concluded that the PCRCG eliminates the active and reactive power ripples under unbalanced grid voltages. Moreover, the oscillations in the DC-link voltage are also eliminated. The elimination of the active and reactive power ripples has several benefits in the grid-tied PV system, such as it reduces the power losses, increases the power efficiency of the PV array and increases the life span and reliability of the PV panels.

4.5 Experimental Validation

The experimental tests are conducted on a laboratory prototype of 3.65 kW using an OPAL-RT real-time simulator RT-LAB OP4510. The system’s control parameters are given in Table 4.1 and the photograph of the experimental setup is shown and Fig. 4.12. The three-phase inverter is realized using six insulated gate bipolar junction transistor (IGBT) modules SKM 150 GB 12T4 (Semikron make). The firing pulses from the APMR controller are given to the IGBTs through skyper 32 gate drivers. The PV array simulator CHROMA 62050H-600S is used to realize the PV arrays, which are connected to the grid simulator ITEC GS010 415-16 via VSI. The system performance of the proposed PLL-less APMR control strategy is compared with the PLL-based CPMR control strategy. The grid-tied PV system performance has been analyzed for adverse conditions such as grid voltage harmonic distortions, grid voltage sag and swells, and grid frequency variations.

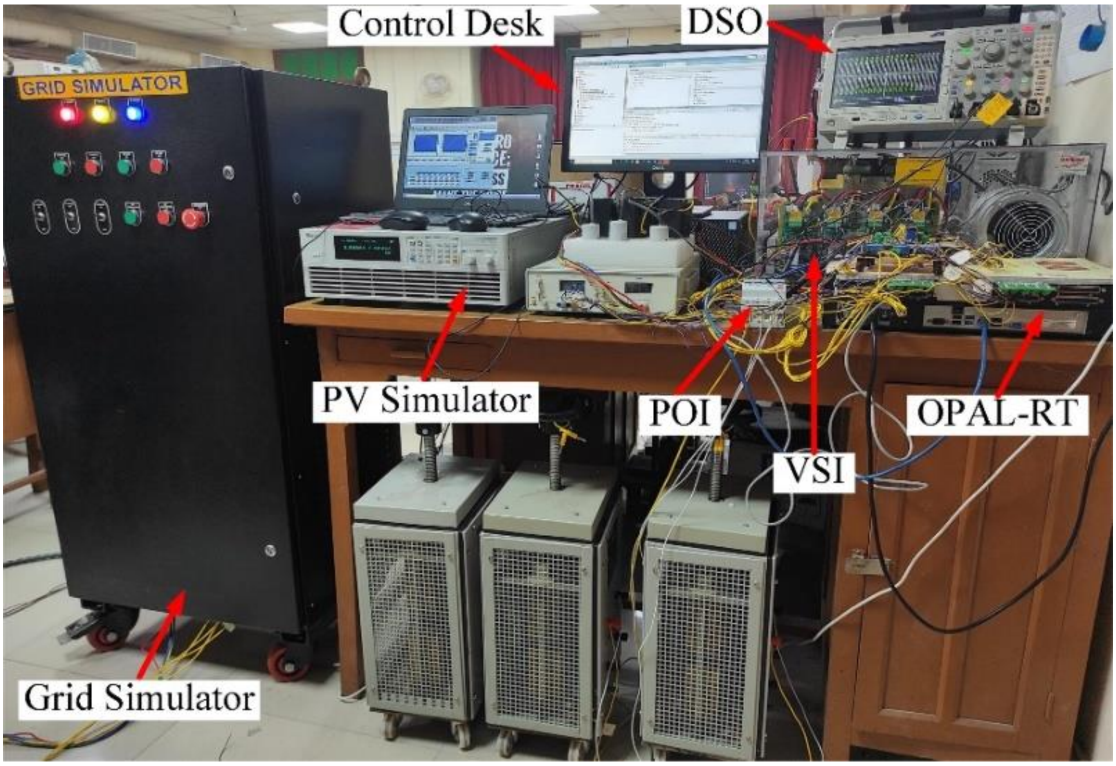

Fig. 4.12. Photograph of the laboratory prototype.

Table 4.1. Real-time System and Control Parameters

	Description	**Symbol**	**Value**
System Parameters	Grid voltage amplitude	V_g	110 V (L-L rms)
	Grid frequency	f_g	50 Hz
	Switching frequency	f_s	20 kHz
	Grid inductance	L_g	1.2 mH
	Inverter side impedance	L_{if} , R_{if}	6.2 mH,0.037 Ω
	Filter capacitance	C_f	10 µF
	Grid side impedance	L_{of}, R_{of}	1.6 mH, 0.016 Ω
	DC link capacitance	C_{dc}	4700 µF
	PV open circuit voltage	V_{PVoc}	443.0 V
	PV short circuit current	I_{PVsc}	10.26 A
	PV MPP voltage	V_{MPP}	380 V
	PV MPP current	I_{MPP}	9.60 A
	PV Maximum power	P_{MPP}	3.65 kW
Control Parameters	PI controller (DC-link voltage controller)	K_{pvdc} , K_{ivdc}	5, 80
	APMR controller	K_p, K_{rA}, K_{rB}, ξ, ω_b	60, 360, 360, 0.02, 6.28 rad/s

4.5.1 Performance Assessment with Grid Voltage Harmonics Distortions

In this section, the proposed PLL-less APMR control strategy's effectiveness has been demonstrated under harmonically distorted grid voltages. The grid voltage is made highly distorted by the typical 5th, 7th, 11th, 13th, 17th and 19th order harmonics, whose magnitudes are 10%, 10%, 6%, 6%, 2% and 2% respectively with respect to the fundamental component. The dynamic waveforms of the grid currents i_{gabc} and grid voltages v_{gabc} before and after enabling the control strategy are shown in Fig.4.13(a)-(c). It is observed that the injected grid currents are highly distorted due to severe grid voltage distortion before enabling the control strategy. Fig.4.13(b) shows that after enabling the control strategy with the PLL-less APMR, the grid current is almost sinusoidal, and the grid current harmonics are suppressed effectively. However, with the PLL-based CPMR control strategy, the i_{gabc} are still non-sinusoidal after enabling the control strategy, as shown in Fig. 4.13(c). The harmonic current spectrum of the grid current without compensation, with PLL-based CPMR control strategy and proposed PLL-less APMR control strategy are shown in Fig. 4.14. When the compensation is disabled, the THD of grid current is 8.43%. When the compensation is enabled with PLL-based CPMR control strategy, the THD is decreased to 7.49%. However, with the proposed PLL-less APMR control strategy, the THD is decreased to 3.3%, which is within the stipulated limit (5%) of IEEE 519 standards [125]. Thus, the proposed PLL-less APMR control strategy shows better grid current harmonic suppression capability than the PLL-based CPMR control strategy.

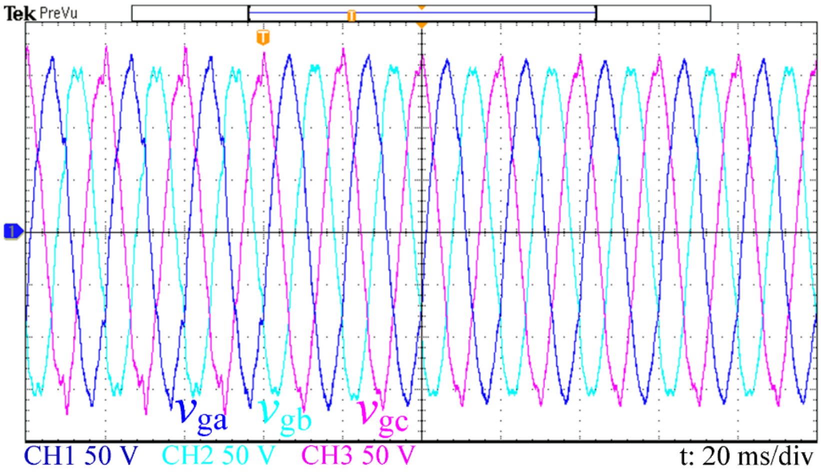

(a)

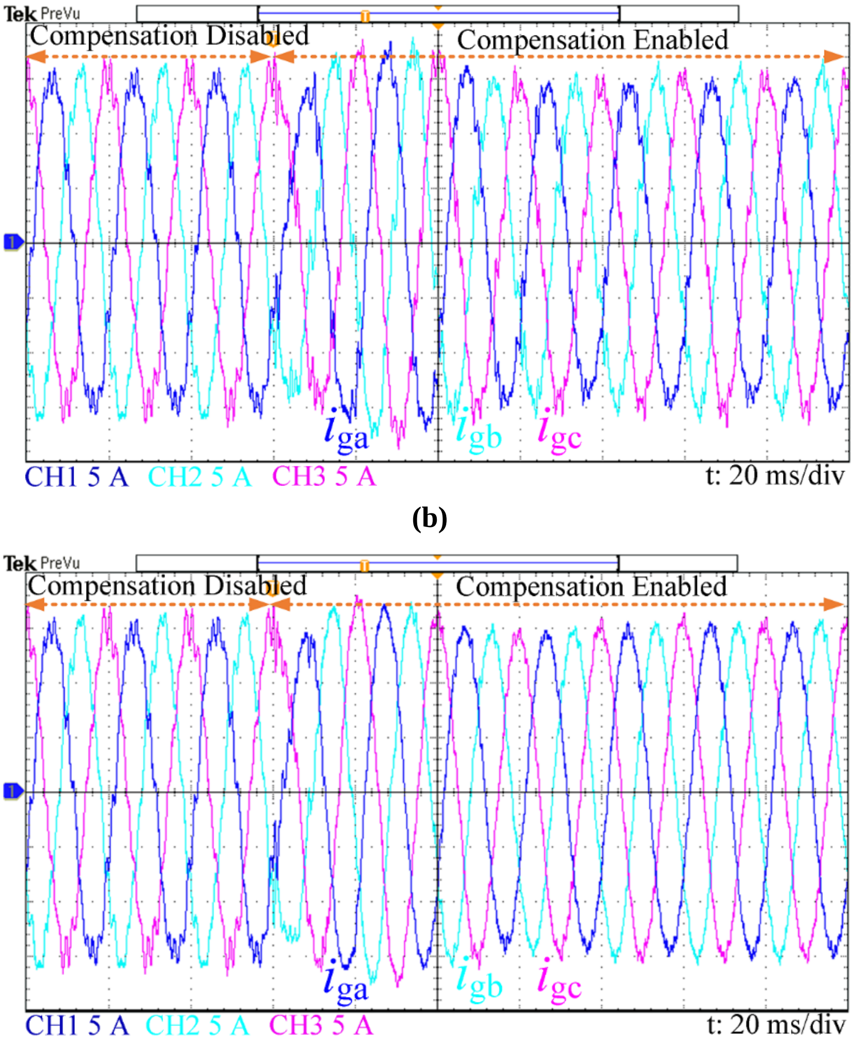

(b)

(c)

Fig. 4.13. Dynamic real-time waveforms when compensation is disabled and enabled **(a)** grid voltages (v_{gabc}) **(b)** grid currents (i_{gabc}) obtained by PLL-based CPMR control strategy **(c)** grid currents (i_{gabc}) obtained by the proposed PLL less APMR control strategy.

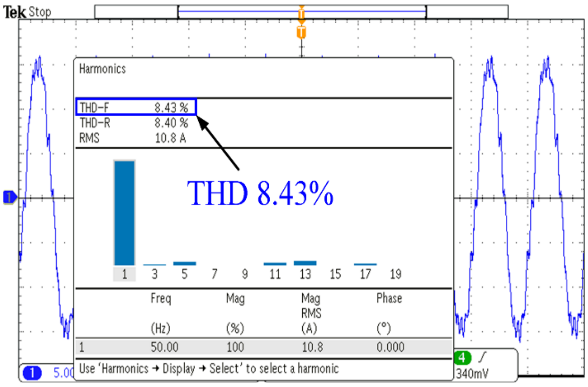

Harmonics

THD–F 8.43 %
THD–R 8.40 %
RMS 10.8 A

	Freq (Hz)	Mag (%)	Mag RMS (A)	Phase (°)
1	50.00	100	10.8	0.000

Use ‘Harmonics → Display → Select’ to select a harmonic

(a)

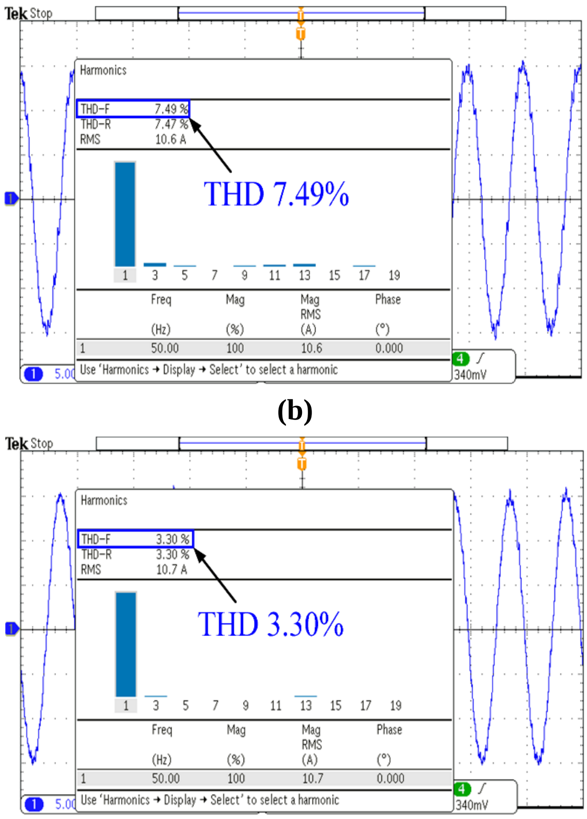

(b)

(c)

Fig. 4.14. The spectrum of experimental grid current under different compensation methods **(a)** when compensation is disabled **(b)** when compensation is enabled using PLL based CPMR control strategy **(c)** when compensation is enabled using proposed PLL less APMR control strategy.

4.5.2 Performance Assessment with Grid Voltage Sag and Swell Under Varying Solar Irradiance

In this section, the performance of the proposed PLL-less control strategy is verified during voltage sag and swell, and irradiance S_{ir} variation. Fig. 4.15 illustrates the experimental waveforms of the grid-tied PV system with grid voltage sag and change in S_{ir} obtained by the proposed PLL-less APMR and PLL-based CPMR control strategies. It can be seen from Fig. 4.15(a) that a single-phase voltage sag of 40% occurs in phase a at t = 40 ms and the grid voltage restores to the rated normal value at t = 360 ms. At t = 120 ms, the S_{ir} is increased from 1000 W/m^2 to 1400 W/m^2. Figs. 4.15(b)-(c) show grid currents obtained by PLL-based CPMR and the proposed PLL-less APMR control strategies, respectively. It is observed that the grid current increases during the interval t = 40 ms to 120 ms, due to the decrease in grid voltage in order to maintain constant power operation. It is seen that during the interval t = 120 ms to 360 ms, the grid current again increases due to the increase in solar irradiance. The grid current is close to sinusoidal and balanced during the interval t = 40 ms to 360 ms using the proposed PLL-less APMR control strategy with PCRCG as compared to the PLL-based CPMR control strategy. Figs. 4.15(d)-(e) show the grid injected real and reactive powers, PV voltage and PV power for PLL-based CPMR and proposed PLL-less APMR control strategies, respectively. During the voltage sag, grid injected active power and PV voltage oscillates significantly using the PLL-based CPMR control strategy. However, with the proposed PLL-less APMR control strategy, oscillations in PV voltage active and reactive powers are almost eliminated.

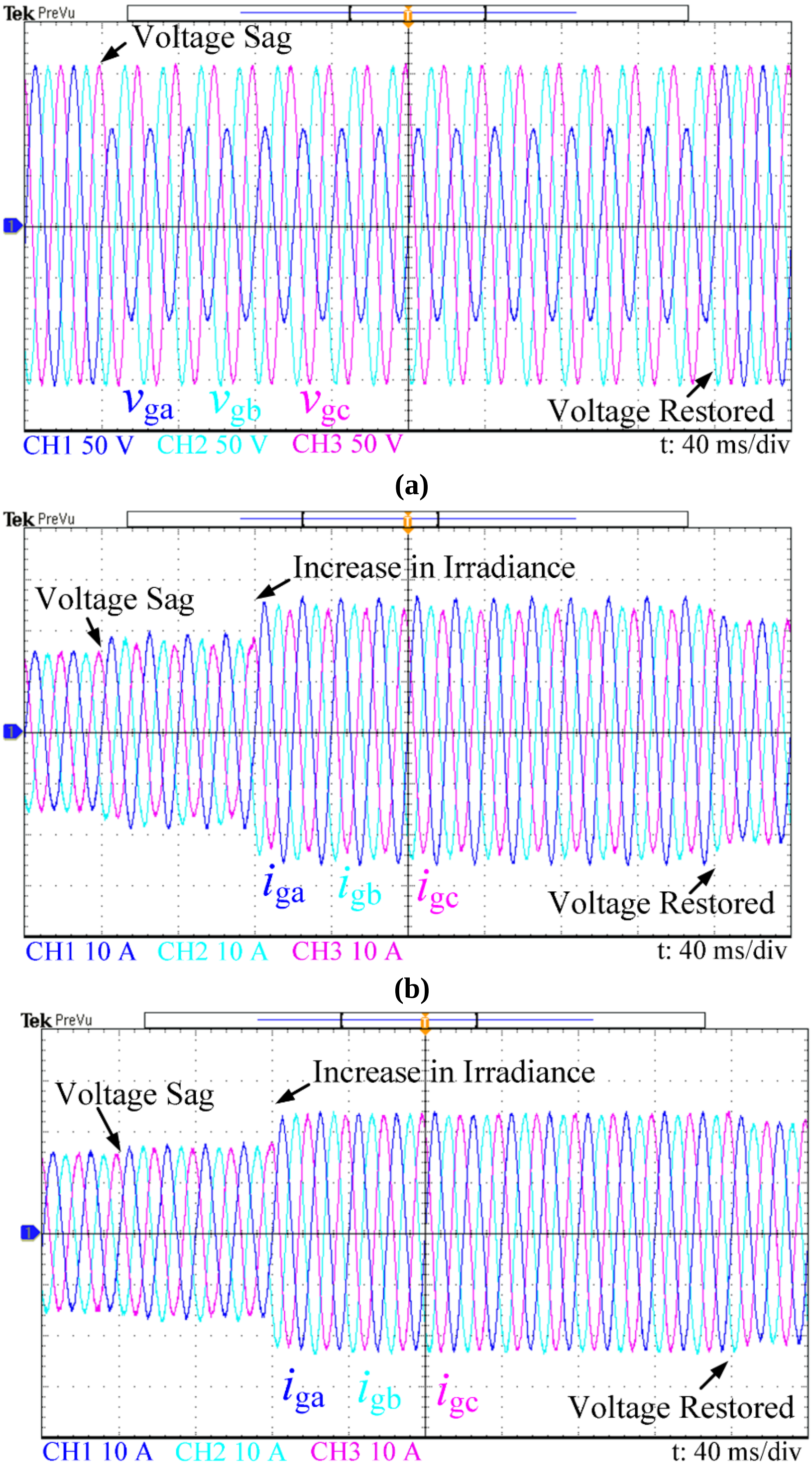

(a)

(b)

(c)

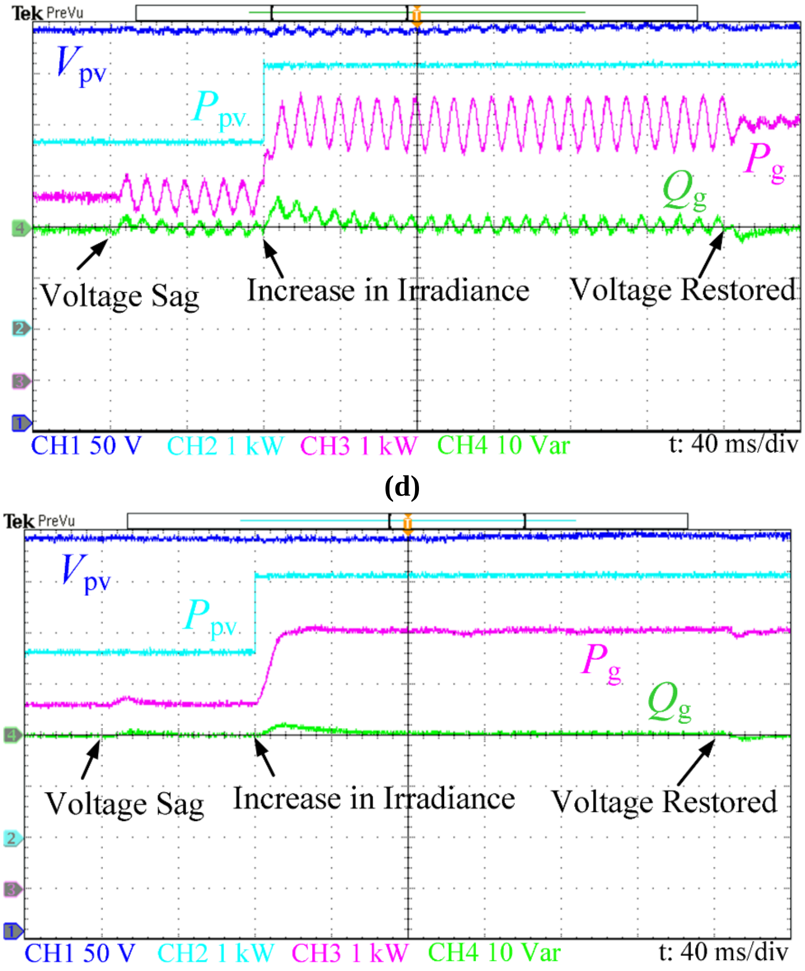

(d)

(e)

Fig. 4.15. Experimental waveforms when applying a 40 % voltage sag in phase *a* and irradiance S_{ir} increases from 1000 W/m^2 to 1400 W/m^2 **(a)** grid voltages v_{gabc} **(b)-(c)** grid currents i_{gabc} obtained by the PLL based CPMR control strategy and proposed PLL less APMR control strategy respectively **(d)-(e)** PV voltage V_{pv}, PV power P_{pv}, active and reactive power injected to the grid obtained by the PLL based CPMR control strategy and proposed PLL less APMR control strategy respectively.

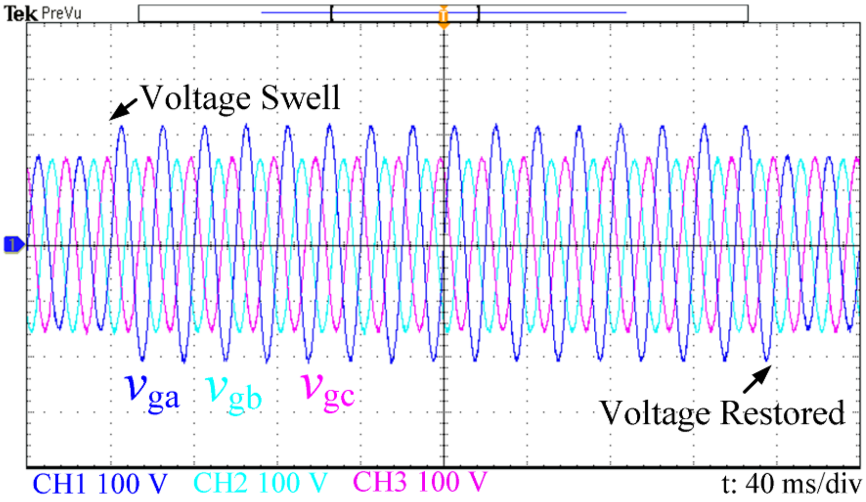

(a)

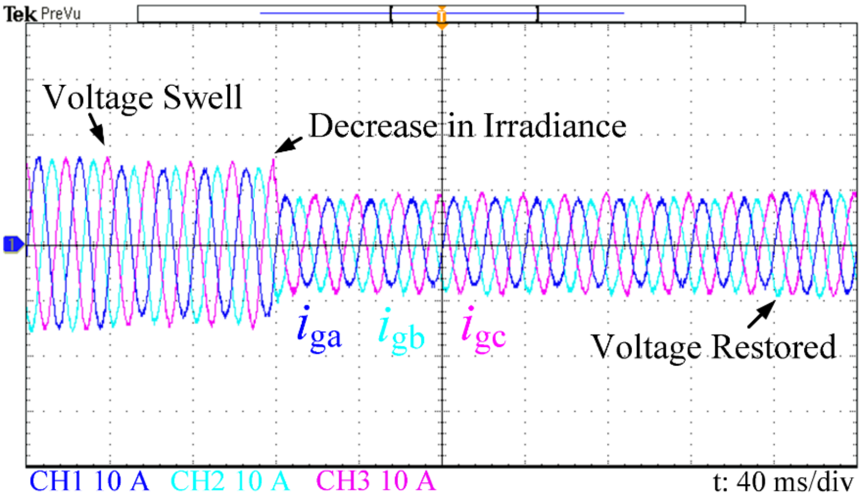
Tek PreVu
Voltage Swell
Decrease in Irradiance
i_{ga}
i_{gb}
i_{gc}
Voltage Restored
CH1 10 A
CH2 10 A
CH3 10 A
t: 40 ms/div

(b)

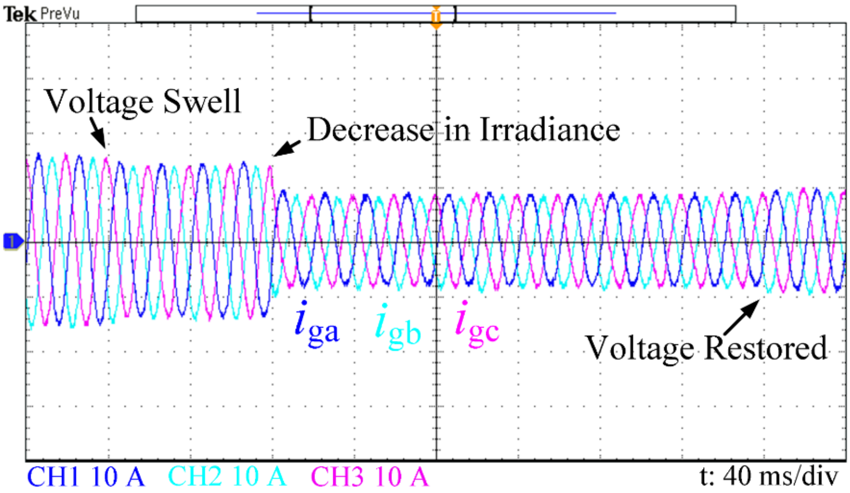
Tek PreVu
Voltage Swell
Decrease in Irradiance
i_{ga}
i_{gb}
i_{gc}
Voltage Restored
CH1 10 A
CH2 10 A
CH3 10 A
t: 40 ms/div

(c)

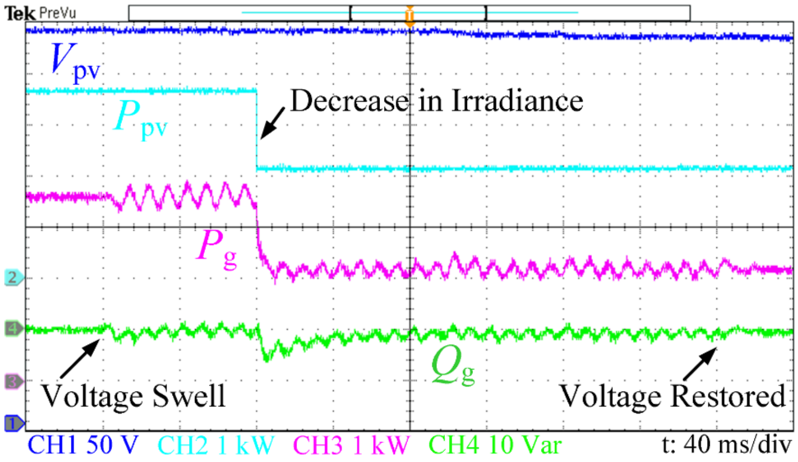
Tek PreVu
V_{pv}
P_{pv}
Decrease in Irradiance
P_g
Q_g
Voltage Swell
Voltage Restored
CH1 50 V
CH2 1 kW
CH3 1 kW
CH4 10 Var
t: 40 ms/div

(d)

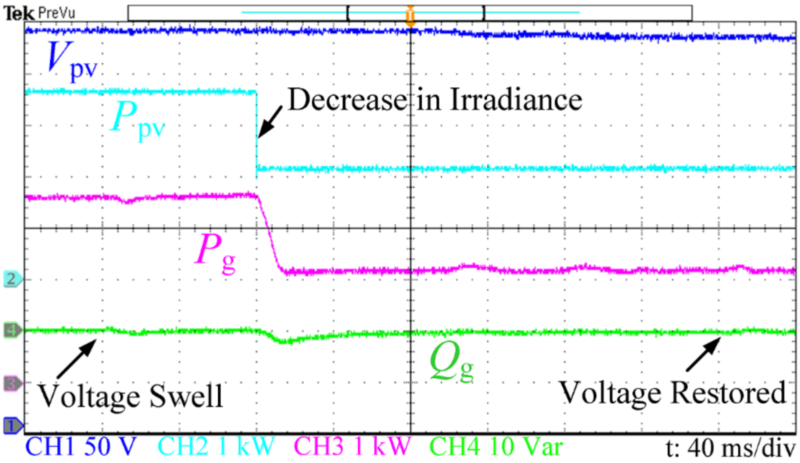

(e)

Fig. 4.16. Experimental waveforms when applying a 35% voltage swell in phase *a* and irradiance S_{ir} decrease from 1000 W/m^2 to 600 W/m^2. **(a)** grid voltages v_{gabc} **(b)-(c)** grid currents i_{gabc} obtained by the PLL based CPR control strategy and proposed PLL less APMR control strategy **(d)-(e)** PV voltage V_{pv}, PV power P_{pv}, active and reactive power injected to the grid obtained by the PLL based CPMR control strategy and proposed PLL less APMR control strategy.

Similarly, the performance analysis of grid-tied PV system with grid voltage swells and change in S_{ir} is carried out using the proposed PLL-less APMR and PLL-based CPMR control strategies. As seen from Fig. 4.16 (a) at t = 40 ms, the grid voltage swell occurs in phase *a* with 35% of its normal value and the grid voltage is recovered to its normal value at t =360 ms. At t = 120 ms, S_{ir} decreases from 1000 W/m^2 to 600 W/m^2. It is observed from Figs. 4.16(b)-(c) that during the interval t = 40 ms to 120 ms, the grid current with both PLL-based CPMR and proposed PLL-less APMR control strategies is decreased due to grid voltage swell. The grid current decreases due to decreased solar irradiance during the interval t = 120 ms to 360 ms. The grid current is close to sinusoidal using the proposed PLL-less APMR control strategy than the PLL-based CPMR control strategy. It is seen from Fig. 4.16(d) that the active and reactive powers oscillate at twice of the grid frequency, using the PLL-based CPMR control strategy. However, with the proposed control strategy, the active and reactive power oscillations are almost eliminated as shown in Fig. 4.16(e). It is observed from Figs. 4.16(d)-(e) that the PV voltage decreases slightly, which decreases the PV power due to a decrease in solar irradiance.

4.5.3 Performance Assessment with Grid frequency Variations

The dynamic performance of the grid-tied PV system using the conventional PLL-based CPMR and the proposed PLL-less APMR control strategies during the grid frequency variation from 49 Hz to 51 Hz is shown in Fig. 4.17. It can be noticed from Fig. 4.17 (a) that the effect of grid frequency change is taken care of by the PLL-based CPMR control strategy within 5 cycles (100 ms). However, the proposed PLL-less APMR control strategy takes care the frequency change in grid frequency within a cycle (20 ms) as shown in Fig. 4.17(b). Thus, it is concluded that the proposed PLL-less APMR control strategy ensures improved dynamic performance as compared to PLL-based CPMR control strategy under grid frequency variations.

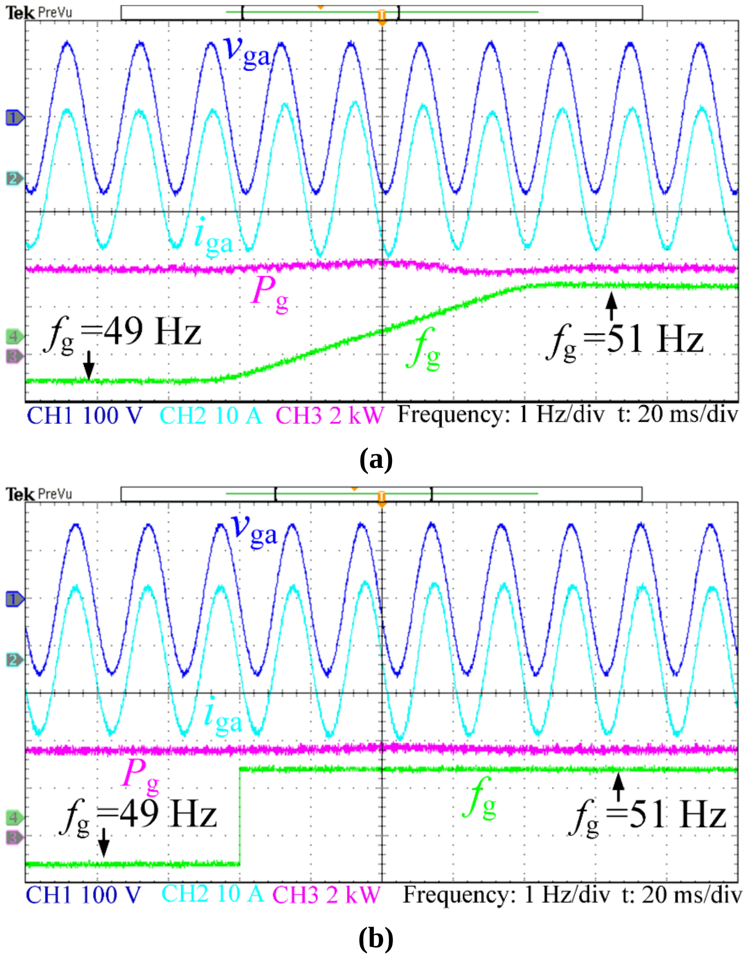

(a)

(b)

Fig. 4.17. Dynamic experimental waveforms during a grid frequency deviation from 49 Hz to 51 Hz obtained by [grid voltage v_{ga}; grid current i_{ga}; grid injected active power P_g; grid injected reactive power Q_g; grid frequency f_g] **(a)** PLL based control with conventional PMR controller **(b)** proposed PLL less control with APMR controller.

4.5.4 Tracking Performance Assessment with Adaptive Step-Size INC MPPT

The system's dynamic response with the adaptive step-size INC MPPT is shown in Fig. 4.18 with variation in irradiance, temperature and reactive power reference. The initial DC-link voltage V_{PV} is 310 V and the corresponding PV array power P_{PV} is 3.2 kW at solar irradiance S_{ir} = 1000 W/m^2 and temperature T = 25 °C. The initial grid injected reactive power Q_g is zero. The MPPT controller is enabled at $t = t_1$ and the PV voltage reaches the maximum power point voltage V_{MPP} = 380 V, when the P_{PV} is 3.65 kW at MPP. The MPP tracking time $t_{\mathrm{MPP1}} = 1.12$ s. At $t = t_2$, the environmental condition is suddenly changed from $S_{\mathrm{ir}} = 1000$ W/m^2, $T = 25$ °C to $S_{\mathrm{ir}} = 850$ W/m^2, $T = 45$ °C. The V_{PV} and P_{PV} reach to new MPP ($V_{\mathrm{PV}} = 340$ V and $P_{\mathrm{PV}} = 3.35$kW) with MPP tracking time $\mathrm{t}_{\mathrm{MPP2}} = 0.96$ s. At $t = t_3$, the reactive power reference Q_{gref} is changed from 0 to 1.5 kVar, and the injected reactive power to the grid Q_{g} is changed from 0 to 1.5 kVar. With a change in Q_{g}, the disturbances in V_{PV} and P_{PV} are insignificant due to the decoupling between the controllers.

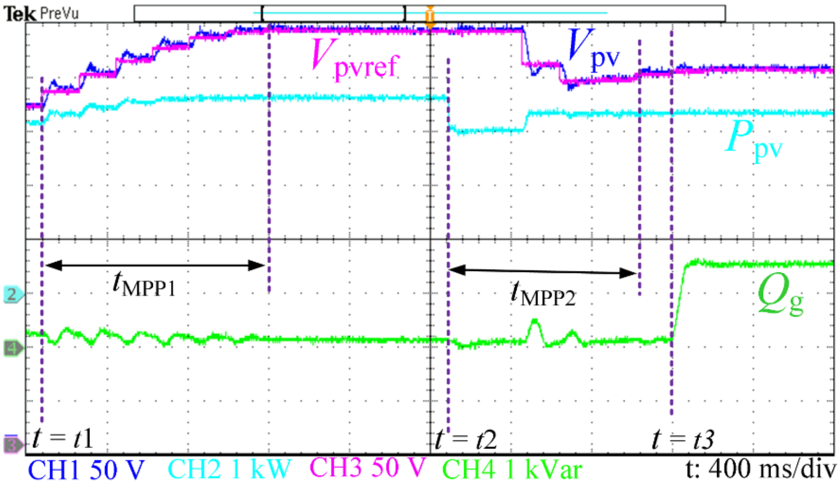

Fig. 4.18. Dynamic performance evaluation of the grid-tied PV system with the ASINC MPPT: PV voltage V_{PV}, PV voltage reference V_{PVref}, PV power P_{PV}, grid injected reactive power Q_{g}.

4.5.5 Comparative Assessment of the Proposed Control Strategy with the Existing Control Strategies

The comparative analysis of the proposed PLL-less APMR control strategy with the other existing control strategies is presented in Table 4.2. The comparison table shows the effectiveness of the proposed PLL-less APMR control strategy in terms of various parameters. It is observed that the proposed PLL-less APMR control strategy exhibit less execution time 0.9 µs and computational burden of 3.66% as compared to the PLL-based CPMR control strategy with execution time 1.9 µs and computational burden of 7.12%. As the proposed PLL-less APMR control strategy uses basic arithmetic calculations, such as addition, subtraction and multiplication that consume a very low computational burden on the OPAL-RT simulator, the proposed control strategy is simpler as compared to the existing control strategies. Further, with the proposed PLL-less APMR control strategy, the frequency tracking capability is better than the PLL-based CPMR control strategy. The THD of the grid current using vector current control based direct power control (VCCDPC) and PLL-based CPMR control strategies are 8.43% and 7.49%, respectively. However, the grid current THD using the proposed PLL-less APMR control strategy is 3.3%, which is significantly lower than other control strategies. It is observed that with the PLL-based

CPMR control strategy, the peak-to-peak active power ripple during grid voltage sag is 0.8 kW, which is 23% of the rated grid injected active power 3.5 kW. However, with the proposed PLL-less APMR control strategy, the active power ripple is very low 0.015 kW, which is 0.43% of the rated grid injected active power 3.5 kW. It is observed from Table 4.2 that the proposed PLL-less APMR control strategy is superior as compared to the existing control strategies in terms of implementation complexity, computational burden, faster adaptability to frequency variations, improved current THD during harmonically distorted grid voltages and reduced power oscillations during the voltage sag.

Table 4.2. Comparative Analysis of The Proposed PLL-Less Control Strategy With Existing Control Strategy

Features	PLL based CPMR control strategy [126]	Vector current control based direct power control [120]	GCPPP without phase angle synchronization [127]	Proposed PLL-less APMR control strategy
PLL requirement	Required	Not required	Not required	Not required
Harmonics elimination	Good	Poor	Not reported	Very good
Power oscillations	High	Medium	Medium	Very Low
Frequency tracking capability	Low	Better	Better	Better
MPPT tracking	Not reported	Not reported	Not reported	Reported
Performance under distorted grid voltages	Affected	Affected	Affected	Not affected
Computational burden	High	Medium	Medium	Low
Implementation Complexity	Complicated	Moderate	Moderate	Simple
Memory requirement for micro controller	Very high	Medium	Medium	Low
Dynamic performance	Poor	Good	Good	Better
THD of grid currents	7.49 %	8.43 %	-	3.3 %
Peak to peak active power ripples	0.8 kW	0.6 kW	0.6 kW	0.015 kW
Power ripple (%)	23 %	17 %	17 %	0.43 %
Frequency tracking time	100 ms	2 ms	2 ms	2 ms

Execution time	1.9 μs	1.25 μs	1.4 μs	0.9 μs
Computational burden (%)	7.12 %	4.75 %	5.2 %	3.66 %
Sampling time	25 μs	25 μs	25 μs	25 μs

4.6 Conclusion

A PLL-less integrated control strategy for a single-stage three-phase grid-tied PV system under distorted grid voltages is proposed in this chapter. The proposed control strategy ensures the suppression of grid current harmonics using an APMR controller in integration with the proposed PCRCG, which makes it a compact control structure. The proposed PCRCG eliminates the active and reactive power oscillations during grid voltage sags and swells effectively. The synchronization task is included within the PCRCG, which makes it PLL-less grid-tied PV system. With the elimination of PLL and thus not requiring the Park's transformation, the computational burden is significantly reduced in case proposed control strategy. To verify the effectiveness of the proposed control strategy, a laboratory prototype is developed and tested for 3.65 kW PV power. It can be observed from the experimental observations that as compared with the PLL-based CPMR control strategy, the proposed PLL-less APMR control strategy is more effective in mitigating the grid current harmonics and eliminating the power ripples under distorted grid voltage conditions. Furthermore, with the proposed PLL-less control strategy, the frequency adaptability of the grid-tied PV system is enhanced during grid frequency variations.

During the grid fault condition, the grid-tied PV system requires achieve LVRT capability. Moreover, under weak grid conditions the dynamics of the grid-tied PV system becomes complicated which may lead to system stability. In these conditions, the proposed PLL-less APMR strategy integrated with PCRCG suffers from performance and stability issues. To effectively suppress the injected grid current harmonics and to improve the LVRT capability of the grid-tied PV system under weak grid conditions, an advanced PLL-less control strategy is presented in chapter 5.